

PNNL-38243

Developments in Processing Criteria for Iron Phosphate Waste Form Design for Treating Electrorefiner Salt Wastes

September 2025

Harmony S. Werth
Krista Carlson (UNR)
Jade Beland (UNR)
Julian D Escobar Atehortua
Paige Murray (UNR)
Dave Liang (UNR)
Laurel Sharpless (UNR)
Brian J. Riley
Michael Simpson (UU)
Charmayne Lonergan (MUST)



DISCLAIMER

This report was prepared as an account of work sponsored by an agency of the United States Government. Neither the United States Government nor any agency thereof, nor Battelle Memorial Institute, nor any of their employees, makes any warranty, express or implied, or assumes any legal liability or responsibility for the accuracy, completeness, or usefulness of any information, apparatus, product, or process disclosed, or represents that its use would not infringe privately owned rights. Reference herein to any specific commercial product, process, or service by trade name, trademark, manufacturer, or otherwise does not necessarily constitute or imply its endorsement, recommendation, or favoring by the United States Government or any agency thereof, or Battelle Memorial Institute. The views and opinions of authors expressed herein do not necessarily state or reflect those of the United States Government or any agency thereof.

PACIFIC NORTHWEST NATIONAL LABORATORY

operated by

BATTELLE

for the

UNITED STATES DEPARTMENT OF ENERGY

under Contract DE-AC05-76RL01830

Printed in the United States of America

Available to DOE and DOE contractors from the Office of Scientific and Technical Information, P.O. Box 62, Oak Ridge, TN 37831-0062

ph: (865) 576-8401 fox: (865) 576-5728 email: reports@osti.gov

Available to the public from the National Technical Information Service 5301 Shawnee Rd., Alexandria, VA 22312 ph: (800) 553-NTIS (6847) or (703) 605-6000

email: info@ntis.gov
Online ordering: http://www.ntis.gov

Developments in Processing Criteria for Iron Phosphate Waste Form Design for Treating Electrorefiner Salt Wastes

September 2025

Harmony S. Werth
Krista Carlson (UNR)
Jade Beland (UNR)
Julian D Escobar Atehortua
Paige Murray (UNR)
Dave Liang (UNR)
Laurel Sharpless (UNR)
Brian J. Riley
Michael Simpson (UU)
Charmayne Lonergan (MUST)

Prepared for the U.S. Department of Energy under Contract DE-AC05-76RL01830

Pacific Northwest National Laboratory Richland, Washington 99354

Executive Summary

This report describes work done under a Nuclear Energy University Partnership (NEUP) project (UNR contract DE-NE0009317) that included a collaborative effort between Pacific Northwest National laboratory, University of Nevada Reno, University to Utah, and Missouri University of Science and Technology. In this report, the main topics include the following: (1) assessment of H_3PO_4 dechlorination parameters for halide removal from salt simulants, (2) evaluation of crucible compatibility with iron phosphate glass melts (including quartz, alumina, Monofrax K-3, stainless steel 316L, and Inconel 693), and (3) evaluation of waste form properties within a ternary system of P_2O_5 (added as H_3PO_4), Fe_2O_3 and fission product simulants.

Executive Summary ii

Acknowledgments

Pacific Northwest National Laboratory (PNNL) is operated by Battelle Memorial Institute for the U.S. Department of Energy (DOE) under contract DE-AC05-76RL01830. This work was performed under a Nuclear Energy University Partnership (NEUP) Project DE-NE0009317 funded by the U.S. DOE Office of Nuclear Energy under the Material Recover and Waste Form Development (MRWFD) Campaign (NE-43) within the Nuclear Fuel Cycle and Supply Chain (NFCSC) Program. Authors acknowledge William Ebert (Argonne National Laboratory) for running ASTM C1308 chemical durability tests and for technical oversight of the project. Authors also acknowledge Sarrah Dunham-Cheatham (University of Nevada, Reno) for performing inductively coupled plasma mass spectrometry on samples. Authors thank CW Kim (Mo-Sci Corporation, Rolla, MO) for providing the glass frits used in some of the experiments.

Acknowledgments

Acronyms and Abbreviations

A total spectral area

ADP ammonium dihydrogen phosphate (NH₄H₂PO₄)

ANL Argonne National Laboratory

ASTM American Society for Testing and Materials International

BDL below detection limit

BSE backscattered electron (detector)

CCC canister centerline cooling

DOE-NE U.S. Department of Energy Office of Nuclear Energy

DP dechlorinated product

DPF dehalogenated phosphate with Fe₂O₃

DSC differential scanning calorimetry

EDS energy dispersive X-ray spectroscopy

EDTA ethylenediaminetetraacetic acid

ER electrorefiner

ERV3 electrorefiner salt version 3
FWHM full width at half maximum

HPLC high-performance liquid chromatography

ICP-MS inductively coupled plasma mass spectrometry

ID identification (sample)

IS isomer shift

KAS Kissinger-Akahira-Sunose

Meⁿ⁺ cation (with associated charge)

MRWFD Material Recovery and Waste Form Development (Campaign)

MUST Missouri University of Science and Technology

N/A not applicable

NEUP Nuclear Energy University Partnership

NFCSC Nuclear Fuel Cycle and Supply Chain

NL normalized loss

O/P oxygen:phosphorus (molar) ratio

PDF powder diffraction file

PNNL Pacific Northwest National Laboratory

ppm parts per million

QS quadrupole splitting

R universal gas constant

SE secondary electron (detector)

SEM scanning electron microscopy

SS316L stainless steel 316L SSM simple salt mixture

T temperatureTC thermocouple

TGA thermogravimetric analysis

TGA-MS thermogravimetric analyzer mass spectrometer

TRL technology readiness level UNR University of Nevada, Reno

U.S. United States

UU University of Utah
XRD X-ray diffraction

Contents

Acknow	wledgm	ents	iii
Acrony	ms and	Abbreviations	iv
1.0	Introdu	ction	1
2.0	Proces	sing Ranges for Dehalogenation	3
3.0	Evalua	tion of Potential Crucibles Materials	12
	3.1	Quartz	16
	3.2	Alumina	19
	3.3	Monofrax K-3	25
	3.4	Stainless Steel 316L	31
	3.5	Inconel 693	35
4.0	Waste	Form Synthesis	39
5.0	Summa	ary, Conclusions, and Next Steps	50
6.0	Refere	nces	52
Append	dix A –	Additional Characterization Data	.A.1
Figu	res		
rigule	I-1. FI	nuclear fuel (UNF) as well as (b) the process of dehalogenating salt wastes and the process of vitrifying the dehalogenated product into a waste form for disposal. GFC = glass-forming chemicals, TRU = transuranics, and WF = waste form. Reprinted in part with permission from Murray et al. (2024). Copyright 2024 American Chemical Society. Licensed under CC-BY-NC-ND 4.0.	1
Figure	2-1.	Summary of residual CI present in dechlorinated products starting from SSM with experiments performed in air or argon (Werth et al. 2025)	4
Figure	2-2.	(a) The autotitration system (Titroline 7000) connected to the outlet of (b) the tube furnace (MTI Corporation GSL-1600X). In the tube furnace, gas flowed from right to left with any removed byproducts being swept into a Teflon tube, which was inserted into the titration cell shown in (a)	6
Figure	2-7.	Residual chlorine content in the samples with flow rates of 0.1–0.2 L·min ⁻¹ and 2 L·min ⁻¹ measured with ICP-MS used for kinetics studies as measured by ICP-MS.	7
Figure	2-3.	Condensation occurring at the inlet and outlet of the tube furnace for attempted kinetic studies with flow rates of 0.1–0.2 L·min ⁻¹	8
Figure	2-4.	NaOH (mL) consumption by off-gassed byproducts during dechlorination of SSM with P/Cl = 1 for heating rates of 1, 5, and 10°C·min ⁻¹ in air (solid lines) and argon (dashed lines) at 2 L·min ⁻¹ .	9
Figure	2-5.	Conversion of CI resulting from dechlorination of at 1, 5, and 10°C·min ⁻¹ heating rates in air (solid lines) or argon (dotted lines) and gas flow rate of	

Executive Summaryii

Contents

	heating rates of 1°C·min ⁻¹ . Repeated trials for some samples are shown	. 10
Figure 2-6.	Chlorine conversion analyzed using the KAS method for (a) air and (b) argon environments. E_a was derived from the conversion profiles in the 100–200°C and 200–300°C temperature ranges for (c) air and (d) argon	. 11
Figure 3-1.	Schematics of potential options for (left) a continuous process (Dong et al. 2022) and (right) a batch process (Riley et al. 2020) for salt waste treatment.	. 12
Figure 3-2.	(a) Silicon contamination as a function of hold time for samples processed in silica crucibles at 400°C and 600°. (b) Photographs of crucibles after 0 h and 24 h holds at 400°C and 600°.	. 13
Figure 3-3.	Optical images of unaltered coupon materials selected for corrosion study	. 13
Figure 3-4.	(a) A schematic of crucible-melt interaction, (b) the experimental setup before testing, and (c) the bar shown after removal from the melt (alumina bar is shown).	. 14
Figure 3-5.	Pictures of (a) the initial melting of Mo-Sci frit and (b) the foaming that occurred after reaching the glass transition temperature (T_g). Image (b) was color corrected for better visualization. For scale, these crucibles are 53 mm in height (see additional dimensions listed previously)	. 15
Figure 3-6.	The fused quartz-Air-1h sample is shown. The optical image in (a) shows the portion of the fused quartz bar that was in contact with the molten DPF5-336. A BSE image of the bar edge (b) and corresponding EDS map (c) in the meniscus region shows DPF5-336 penetration and transverse cracks.	. 17
Figure 3-7.	The fused quartz-Ar-1h sample is shown. The optical image in (a) shows the portion of the fused quartz bar that was in contact with the molten DPF5-336. A BSE image of the bar edge (b) and corresponding EDS map (c) in the meniscus region shows DPF5-336 penetration and transverse cracks.	. 17
Figure 3-8.	The fused quartz-Air-4h sample is shown. The optical image in (a) shows the portion of the fused quartz bar that was in contact with the molten DPF5-336. A BSE image of the bar edge (b) and corresponding EDS map (c) in the meniscus region shows DPF5-336 penetration and transverse cracks. The blue color in (a) is from the type of epoxy used to mount the sample prior to cutting and polishing.	. 18
Figure 3-9.	The fused quartz-Ar-4h sample is shown. The optical image in (a) shows the portion of the fused quartz bar that was in contact with the molten DPF5-336. A BSE image of the bar edge (b) and corresponding EDS map (c) in the meniscus region shows DPF5-336 penetration and transverse cracks. The blue color in (a) is from the type of epoxy used to mount the sample prior to cutting and polishing.	. 19
Figure 3-10.	The Alumina-Air-1h sample is shown. The optical image in (a) shows a slight divot in either side of the bar at the melt meniscus. The BSE image and EDS maps in (b) reveal the distinct edge between the alumina bar and the residual DPF5-336 at the melt meniscus. An inset dashed box indicates a region shown in (c), showing dendrites in the residual DPF5-	

Figures

	(e) and the linescan in (e) confirm the exclusion of the DPF5-336 from the alumina bar	21
Figure 3-11.	The Alumina-Ar-1h sample is shown. The optical image in (a) shows divots in the bar at the meniscus of the melt. A large divot was investigated with SEM/EDS as shown in (b) and (c), revealing an iron-rich layer between the alumina bar and the residual DPF5-336. BSE Images from the portion of the bar completely submerged in the melt are shown in (d) and (e). The linescan in (e) shows an increased concentration in iron in the layer between the alumina bar and the DPF5-336.	22
Figure 3-12.	The Alumina-Air-4h sample is shown. The image in (a) of the region of the bar at the melt meniscus shows that the bar has separated into two pieces during sample prep. SEM/EDS images in (b) show the distinct edge between the alumina bar and the residual DPF5-336 near the melt meniscus. The bright phase in the residual DPF5-336 is shown in greater detail in (c). Images from the portion of the bar completely submerged in (d) and (e) and the linescan in (e) confirm the exclusion of the DPF5-336 from the alumina bar.	23
Figure 3-13.	The Alumina-Ar-4h sample is shown. The optical image in (a) shows large divots in the bar at the meniscus of the melt. A divot was investigated with SEM/EDS as shown in (b) revealing the distinct edge between the bar and the residual DPF5-336. A closer view of that edge in the divot region in (c) shows extensive formation of dendrites in the residual DPF5-336. The BSE image in (d) from the portion of the bar completely submerged in the melt shows two types of dendrites formed in the residual DPF5-336 along with bright layer at the sample edge. The linescan in (e) shows an increased concentration in iron in the edge layer.	24
Figure 3-14.	The K3-Air-1h sample is shown. The optical image in (a) shows corrosion of the bar in the meniscus region. (b) BSE image showing the bright corrosion layer at the bar edge. Dark regions are voids. The SEM/EDS maps in (c) indicate the penetration of DPF5-336 components beyond the corrosion layer.	26
Figure 3-15.	The K3-Air-4h sample is shown. The optical image in (a) shows corrosion of the bar in the meniscus region with visible penetration of DPF5-336. (b) BSE image showing the bright corrosion layer around light grey areas of DPF5-336. Dark regions are voids. The SEM/EDS maps in (c) indicate the penetration of DPF5-336 components beyond the corrosion layer	27
Figure 3-16.	BSE image showing subsurface corrosion in the submerged region of the K3-Air-4h sample with regions of interest labelled.	28
Figure 3-17.	The K3-Ar-1h sample is shown. The optical image in (a) shows corrosion of the bar in the meniscus region. (b) BSE image showing the bright corrosion layer at the bar edge. Dark regions are voids. The SEM/EDS maps in (c) indicate the penetration of DPF5-336 components beyond the corrosion layer.	29
Figure 3-18.	The K3-Ar-4h sample is shown. The optical image in (a) shows corrosion of the bar in the meniscus region. (b) BSE image of the meniscus region reveals a bright phase along the grain boundaries. The SEM/EDS maps	

Figures

	in (c) confirmed the bright phase contained components from the DPF5-336 glass	30
Figure 3-19.	The SS-Air-1h sample is shown. The optical image in (a) shows extensive corrosion of all surfaces in contact with the molten glass. (b) SEM/EDS maps reveal the migration of components and formation of a corrosion layer. (c) shows the phase separation in the corrosion layer in greater detail.	32
Figure 3-20.	SEM/EDS maps from an area in the submerged region of the SS-Air-1h sample. The edge of the bar that was in contact with the molten glass is oriented to the right. Labels on the left indicate the source of each component.	33
Figure 3-21.	The SS-Ar-1h sample is shown. The optical image in (a) shows extensive corrosion of the bar in the meniscus region. (b) SEM/EDS maps reveal the migration of components and formation of a corrosion layer. (c) SEM of the phase separation in the corrosion layer shown in greater detail	34
Figure 3-22.	The Inconel-Air-1h sample is shown. The sample separated into two pieces during preparation for analysis. The optical image in (a) shows extensive corrosion of all surfaces in contact with the molten glass. The (b) BSE-SEM micrograph of the bar edge and (c) SEM/EDS maps reveal the migration of components and formation of a corrosion layer	36
Figure 3-23.	The Inconel-Ar-1h sample is shown. The optical image in (a) shows extensive corrosion of all surfaces in contact with the molten glass. The (b) BSE-SEM micrograph of the bar edge and (c) SEM/EDS maps reveal the migration of components and formation of a corrosion layer	37
Figure 3-24.	SEM/EDS maps from an area in the submerged region of the Inconel-Ar- 1h sample. The edge of the bar that was in contact with the molten glass is oriented to the right. Labels on the left indicate the source of each component	38
Figure 4-1.	The formation of DPF samples from a simple salt waste simulant is shown in the schematic as a two-step process involving separate dechlorination and vitrification steps	39
Figure 4-2.	Ternary diagram of SSM-DPF target compositions with regions labeled according to the required material additions to the SSM-DP before vitrification. The dashed line indicates target compositions that would require only Fe ₂ O ₃ additions to the SSM-DP. SSM-DPF14 lies on the dashed line. Compositions in the region above the dashed line (colored orange) require the addition of both Fe ₂ O ₃ and alkali carbonates. Compositions in the region below the dashed line (colored blue) require the addition of both Fe ₂ O ₃ and a phosphate precursor (H ₃ PO ₄ was used in this work).	41
Figure 4-3.	Ternary diagram showing the target compositions (mol%) of SSM-DP and SSM-DPFs prepared in this work. Images of the waste forms and their associated sample ID are shown in callouts. Composition markers on the ternary diagram are colored according to their theoretical Fe/P ratio. SSM-DPF7 and SSM-DPF11– SSM-DPF14 were made with an SSM-DP dechlorinated at 600°C and all others were made using an SSM-DP	
	dechlorinated at 400°C	42

Figures ix

Figure 4-4.	SS-DPF10-400 vitrified in (a) air and (b) argon atmospheres. The air sample surface is dark, while the argon sample has a shiny, grey surface with a metallic appearance. It is hypothesized that the difference is caused by a thin crystallized surface layer such as Fe ₂ O ₃ for the sample prepared in argon based on similar observations from a previous study (Riley et al. 2020).	43
Figure 4-5.	XRD scans of SSM-DPFs show four amorphous samples as labelled	43
Figure 4-6.	SEM images and EDS maps of the cross-sections of (a) SSM-DPF9-400 (b) SSMDPF-10-400 and (c) SSM-DPF8-400. The dashed boxes in (c) show the corresponding BSE image boundary. All samples show phase-separated Si droplets.	44
Figure 4-7.	Simultaneous DSC/TGA of SSM-DPF10-400. Dashed lines mark the temperatures of the glass transition temperature (T_g), the onset of crystallization (T_x), and the melting temperature (T_m)	46
Figure 4-8.	Mössbauer spectrum of SS-DPF10-400 with the results in the inset table	47
Figure 4-9.	Graphs showing mass loss of SSM-DPFs in the dissolution scoping test with (a) showing all samples tested and (b) showing the magnified region of the grey area. Samples with the same composition are shown in the same color. Square markers indicate SSM-DPF-600 samples, while circular markers indicate SSM-DPF-400 samples. Two samples were tested for SSM-DPF4-400: one sample from the crystalline half, one from the glassy half, which is shown with a filled marker. SSM-DPF10-600 had no measurable mass loss during the testing period. Markers indicate measured values; dashed lines are a guide for the eye	48
Figure 4-10.	Cumulative normalized elemental mass loss values as a function of time for ASTM C1308 test with SSM-DPF10-400. The linear regression of values from each species are shown as solid lines	49
Figure 4-11.	SSM-DPF10-400 before and after the ASTM C1308 leaching test. Grey spots appeared on the surface of the sample during leaching. Both samples are shown mounted in epoxy and have separate scale bars	
Tables		
Table 2-1.	Composition of the simple salt mixture (SSM) and electrorefiner salt simulant version 3 (ERV3)	3
Table 2-2.	Theoretical dechlorination reactions based on cation valence of the chloride salt and phosphate precursor species. Eq. (1) – Eq. (3) apply to processing with ADP and Eq. (4) – Eq. (6) apply to processing with H ₃ PO ₄ . Here, Me ⁿ⁺ denotes the salt cation	3
Table 2-3.	Dechlorination efficacy shown as remaining chlorine (mass%) for a SSM with P/Cl = 1	4
Table 2-4.	Evaluation of the temperature difference (set temperature = 300°C) from the furnace temperature controller (TC1) and an inserted, removable temperature controller (TC2) for 0.1–0.2 L·min ⁻¹ and 2 L·min ⁻¹ samples in air, highlighting the impact of the flow rate on the final temperature of the furnace	7

Tables

Table 3-1.	Composition of the binary iron phosphate glass frit produced by Mo-Sci Corporation for corrosion studies.	14
Table 3-2.	Summary of corrosion of bars in molten DPF5-336. The corroded area was determined by OM in the 13.8 mm region around the neck. Oxide depth, penetration depth, and crack depth were determined with SEM-EDS. Penetration depth includes the oxide depth. N/A = not applicable, with footnotes below the table with additional details, ID = identification	16
Table 3-3.	Concentration of selected elements in different regions of the residual DPF5-336 in the Alumina-Ar-4h sample as measured by EDS (Figure 3-13d).	25
Table 4-1.	SSM-DP and SSM-DPF target compositions prepared in this study are shown. Calculations assumed all cations in the initial batch form oxides (e.g. all LiCl and Li ₂ CO ₃ in the batch form Li ₂ O) and only trivalent iron is present. A ₂ O denotes total alkali oxide content.	40
Table 4-2.	HPLC results of SSM-DPF10 samples prepared with the indicated dechlorination processing conditions.	47

Tables

1.0 Introduction

This report provides a summary of findings related to the development of processing parameters for iron phosphate waste forms for chloride-based salt compositions, specifically focused on electrorefiner salt compositions. The goal of this work was to process electrorefiner salt wastes from electrochemical processing (*pyroprocessing*) through a halide-removal step (called *dehalogenation*), a high-temperature reaction between the dehalogenated product and glass-forming chemicals (GFCs) at a higher temperature (*vitrification*) into a waste form, and capture of the volatile halide byproducts (e.g., NH₄H₂PO₄, HCl) for recycle. This is described in more detail within Figure 1-1.

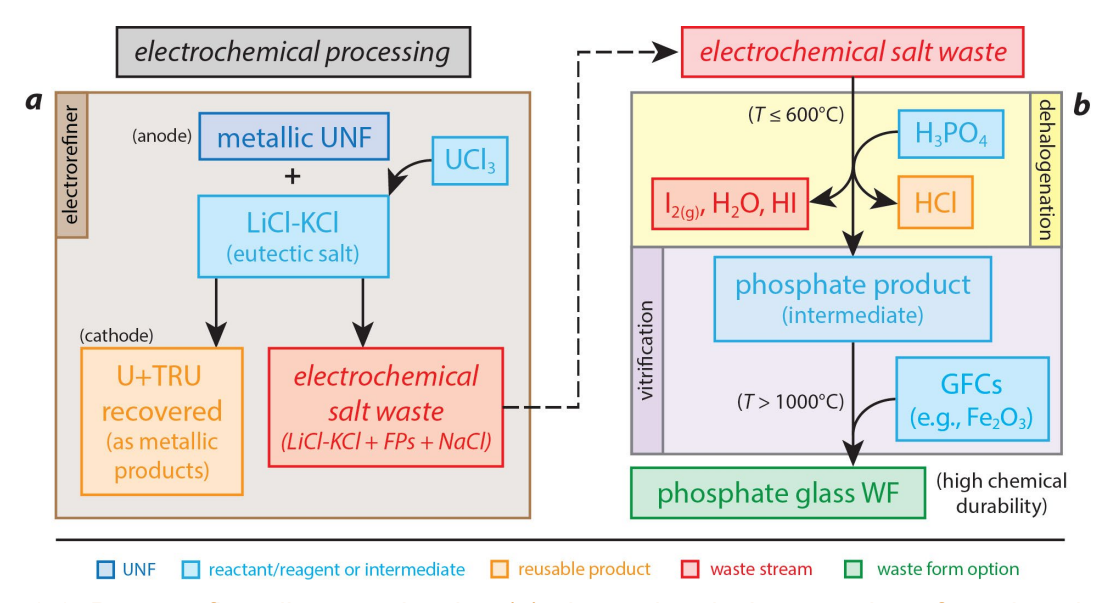


Figure 1-1. Process flow diagram showing (a) electrochemical processing of used nuclear fuel (UNF) as well as (b) the process of dehalogenating salt wastes and the process of vitrifying the dehalogenated product into a waste form for disposal. GFC = glassforming chemicals, TRU = transuranics, and WF = waste form. Reprinted in part with permission from Murray et al. (2024). Copyright 2024 American Chemical Society. Licensed under CC-BY-NC-ND 4.0.

The work reported therein is in direct support of a United States Department of Energy Office of Nuclear Energy (DOE-NE) Nuclear Energy University Partnership (NEUP) Project submitted in response to a 2021 road map report (Riley et al. 2021b) describing the areas in critical needs to advance the Technology Readiness Level (TRL) of the iron phosphate-based waste form process involving dehalogenation of salt wastes. While a summary of published results is included in the document for continuity, the main purpose of the report is to highlight the latest findings that are important and most relevant to advance the TRL in different categories. The research documented in this report focuses on the following objectives to address the most critical needs identified by the road map report:

- (1) Determine processing ranges for electrorefiner (ER) salt simulants in air and argon environments using H₃PO₄. Characterization of the dechlorinated product and the offgassed byproducts were used to understand dechlorination mechanisms and efficacy.
- (2) Examine melt-crucible interactions during dechlorination and vitrification. The corrosive and fluid nature of phosphate melts leads to significant interactions with

Introduction 1

- crucibles used during dehalogenation and vitrification of waste salt into the final iron phosphate waste form. Characterizations of crucible materials and melts were used to provide information about suitability for process equipment.
- (3) Develop phosphate-based waste forms. Originally, the identification of a glass-forming composition was a priority. This was updated as a goal to identify chemically and mechanically stable materials that can be easily formed from the dechlorinated product. This was defined as charging the batch with as few additives as possible, maintaining chemically durable crystalline phases in the vitrified product with glass-forming chemicals added to chemically stabilize the glass.
- (4) Collect glass property-composition data for model development on the glass-forming regions. A glass-forming region for the iron phosphate compositions has been identified. However, phase separation and crystallization are often observed upon canister centerline cooling (CCC) heat treatments. Data is needed on the thermal stability of these glasses and the effects of secondary phase development on durability. Glass forming ability-composition models should be developed for different waste loadings and glass-forming additives (e.g., Fe₂O₃, Al₂O₃), which could differ for each separate salt waste composition.
- (5) Develop a process for reacting the recovered NH₄Cl with metals that need to be fed into the system (e.g., U, Na, Li, K). The secondary off-gas waste produced during processing must be managed and ideally recycled. Recycling will avoid the generation of a secondary waste stream containing Cl and provide a means by which to recharge the systems with UCl₃, which is used as an oxidant in the electrorefiner. This process is particularly needed for a molten salt reactor that may be enriched with costly Cl-37 or be contaminated with long-lived radioactive Cl-36 (t₁/2 = 3.01×10⁵ y). While this topic was a focus of the project, the results from this task are not included within this report. More information can be found in publications by Barnes et al. (2025) and Rood et al. (2024).

Introduction 2

2.0 Processing Ranges for Dehalogenation

Simple salt mixtures (SSM) and version 3 of an electrorefiner salt simulant (ERV3) containing surrogate fission products (Table 2-1) were dechlorinated with phosphate precursors. Studies were primarily performed with phosphoric acid (H_3PO_4) (Murray et al. 2024; Werth et al. 2025). A few studies were conducted with $NH_4H_2PO_4$ (ADP) to compare with previous work (Riley et al. 2020; Riley et al. 2021a; Riley and Chong 2022). The SSM was examined first to provide a homogenous sample to set a range for processing. The ERV3 mixture was provided by Argonne National Laboratory (ANL). The composition ratio of precursor (i.e., H_3PO_4 , ADP) to salt (P/CI) was initially set to the theoretical stoichiometric reactions to enable complete dechlorination based on the salt composition (Table 2-2). All results refer to P/CI = 1 unless stated otherwise.

Table 2-1. Composition of the simple salt mixture (SSM) and electrorefiner salt simulant version 3 (ERV3).

Salt	SSM		ERV3		
Sait	mass%	mol%	mass%	mol%	
LiCI	36.29	48.03	32.00	49.25	
KCI	44.29	33.33	39.00	34.13	
NaCl	19.42	18.64	9.00	10.05	
CsCl	-	-	7.00	2.71	
SrCl ₂	-	-	3.00	1.23	
CeCl ₃	-	-	5.00	1.32	
$NdCl_3$	-	-	5.00	1.30	

Table 2-2. Theoretical dechlorination reactions based on cation valence of the chloride salt and phosphate precursor species. Eq. (1) – Eq. (3) apply to processing with ADP and Eq. (4) – Eq. (6) apply to processing with H_3PO_4 . Here, Me^{n+} denotes the salt cation.

Cation Valence	Reaction Equation	Eq.
Me ⁺¹	$2 \text{ NH}_4\text{H}_2\text{PO}_4 + 2 \text{ MeCl} \rightarrow \text{Me}_2\text{O}\cdot\text{P}_2\text{O}_5 + 2 \text{ NH}_4\text{Cl}(g) + 2 \text{ H}_2\text{O}(g)$	(1)
Me ⁺²	$2 \text{ NH}_4\text{H}_2\text{PO}_4 + \text{MeCl}_2 \rightarrow \text{Me}_2\text{O} \cdot \text{P}_2\text{O}_5 + 2 \text{ NH}_4\text{Cl}(g) + 2 \text{ H}_2\text{O}(g)$	(2)
Me ⁺³	$6 \text{ NH}_4\text{H}_2\text{PO}_4 + 2 \text{ MeCl}_3 \rightarrow \text{Me}_2\text{O}_3 \cdot 3 \text{ P}_2\text{O}_5 + 6 \text{ NH}_4\text{Cl}(g) + 6 \text{ H}_2\text{O}(g)$	(3)
Me ⁺¹	$2 \text{ H}_3\text{PO}_4 + 2 \text{ MeCl} \rightarrow \text{Me}_2\text{O} \cdot \text{P}_2\text{O}_5 + 2 \text{ HCl}(g) + 2 \text{ H}_2\text{O}(g)$	(4)
Me ⁺²	2 H_3PO_4 + $MeCl_2 \rightarrow MeO \cdot P_2O_5$ + $2HCl(g)$ + 2 $H_2O(g)$	(5)
Me ⁺³	$6 \text{ H}_3\text{PO}_4 + 2 \text{ MeCl}_3 \rightarrow \text{Me}_2\text{O}_3 \cdot 3 \text{ P}_2\text{O}_5 + 6 \text{ HCl}(g) + 6 \text{ H}_2\text{O}(g)$	(6)

Dechlorination efficacy and mechanisms were investigated for continuous heating profiles up to 600°C and in air and argon environments. Specifics on sample preparation and details from characterization were reported in previous publications from the team and readers are referred to those documents for more information (Murray et al. 2024; Werth et al. 2025). The major findings from these works are as follows:

- 1) Complete dechlorinations (i.e., below detection limit [BDL] of chlorine using inductively coupled plasma mass spectrometry or ICP-MS) of SSM and ERV3 in air and argon were achieved using H₃PO₄. After a continuous heating profile to the specified terminal temperature (100–600°C), the furnace was shut off and allowed to cool naturally to room temperature.
 - a. For SSM, P/Cl = 1 chlorine concentration was BDL after processing > 500°C (Table 2-3 and Figure 2-1).
 - b. For ERV3, a ratio of P/Cl > 1 was needed to achieve chlorine concentrations at 600°C. For P/Cl = 1, < 2 mass% Cl and for P/Cl = 1.21, the Cl content was BDL.

Table 2-3. Dechlorination efficacy shown as remaining chlorine (mass%) for a SSM with P/CI = 1.

Temperature	Remaining CI (mass%)			
(°C)	Air	Ar		
100	13.8–15.2	19.7–20.0		
200	6.0-6.3	12.1-16.2		
300	0.0-2.3	6.1–6.7		
400	0.7-2.2	0.6-4.3		
500	0.6	0.7-0.8		
600	0.0	0.0-0.6		

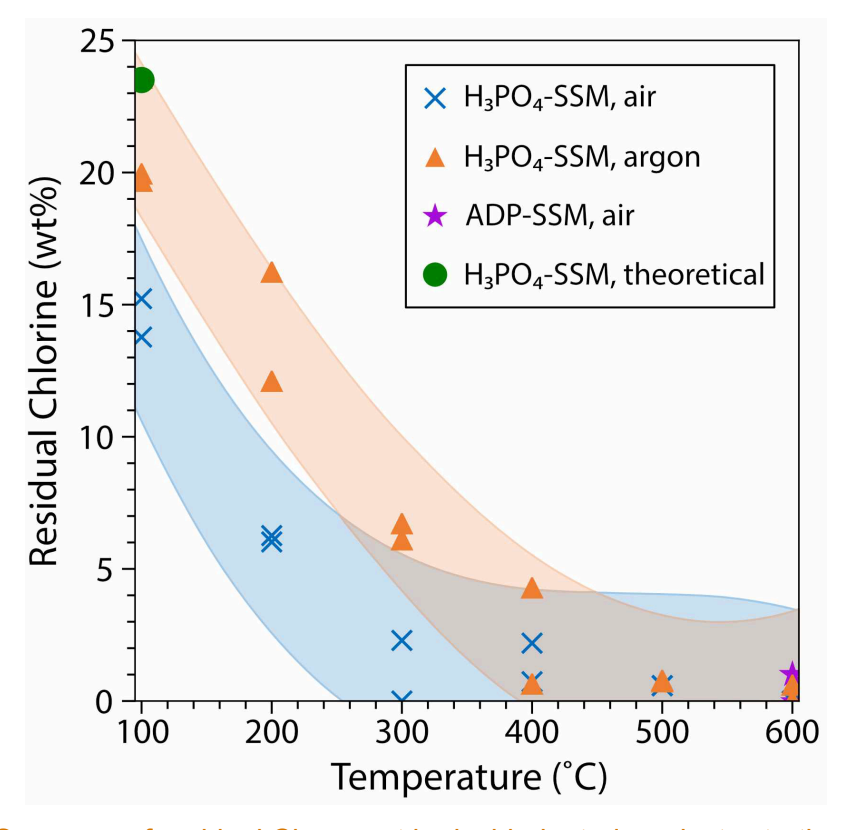


Figure 2-1. Summary of residual CI present in dechlorinated products starting from SSM with experiments performed in air or argon (Werth et al. 2025).

- 2) Oxygen in the environment appears to play a role in dechlorination at $T < 400^{\circ}$ C, where dehydration and condensation reactions of H₃PO₄ dominate. For SSM, > 90 mass% of the chlorine was removed by 300°C, while in Ar, 6–8 mass% CI remained. This information was not yet determined for ERV3.
- 3) Oxygen does not appear to have a significant impact on dechlorination at T > 400°C for SSM and at 600°C for ERV3, i.e., thermally driven reactions related to the evolution of the glass structure.
- 4) Raman analysis showed that samples processed in air had a greater extent of phosphate polymerization than samples processed in Ar by 300°C. Paired with the residual chlorine content, the data indicate that oxygen-assisted polymerization helps release hydrogen to react with chlorine.
- 5) Reactions between the acidic aqueous solution and ERV3 during heating are more complex than the SSM due to the presence of the trivalent lanthanides. Polyphosphate chains, likely terminated with hydroxide groups, favored the formation of insoluble oxides and retention of chlorine anions at higher processing temperatures.
- 6) ERV3 samples with P/Cl = 1 and processed at 600°C were opaque. A monazite phase, specifically (Sr,Nd,Ce)(PO₄)₃ (PDF 00-056-0893), was identified with X-ray diffraction (XRD). Dechlorinated samples became increasingly transparent and X-ray amorphous with increasing P/Cl ratios. Full transparency was typically achieved in air by P/Cl = 1.16 and in argon by P/Cl = 1.21. However, this was variable due to heterogeneity of the salt composition.
- 7) Retaining monazite (or any insoluble crystalline oxide) in the final waste form will be advantageous if the alkali phosphate matrix can be chemically stabilized with an additive. More work was documented on the benefits of monazite and xenotime elsewhere (Chong et al. 2024).
- 8) The only components observed in the off-gas stream when processing with H_3PO_4 were HCl(g) and $H_2O(g)$ with the highest release rate of both gases occurring at $\approx 100^{\circ}C$.
- 9) Using H₃PO₄ instead of ADP for dechlorination could be advantageous to minimize foaming and reduce complexity of the off-gas stream. However, if it is desirable to start with solid powders and/or capture the off-gas stream as solid a condensate, a system could be designed to use ADP to mitigate foaming and decomposition of the NH₄Cl(s) byproduct.
- 10) Silicon contamination in the melt from the silica crucibles used was observed after dechlorination and does not appear to depend on the atmosphere. There is a fairly linear trend of increasing Si content with increasing temperature, with contamination levels ranging from 0.02 mass% to 0.10 mass% after processing at 100°C and 600°C, respectively, as examples.
- 11) Crucibles used for processing SSM at $T \le 400^{\circ}$ C did not fracture upon cooling $T < 100^{\circ}$ C, but those processed at $500-600^{\circ}$ C fractured $\approx 50\%$ of the time. None of the silica crucibles used for processing ERV3 fractured upon cooling. Additional studies are needed to determine how the multivalent cations in the glass assist in mitigating crucible fractures. The exact cause of the fracturing was not determined.

Based on these initial results, additional information was collected on the effects of heating profile, atmosphere, and flow rate on reaction kinetics.(Beland 2025) Based on the previous results, studies were conducted using batches prepared in silica crucibles (AdValue, high form, FQ-1050) composed of SSM and a ratio P/CI = 1 as reported in previous publications.(Murray et al. 2024; Werth et al. 2025) The furnace (MTI Corporation, GSL 1600X) was prepared with a heating profile terminating at 300°C and a flow rate of 2 L·min⁻¹ to ensure dechlorination products were swept soon after release. At lower flow rates, such as 0.1-0.2 L·min⁻¹, byproducts were retained in the furnace, causing condensation on the inlet and the outlet of tube furnace (Figure 2-3). Testing was conducted in a tube furnace (Figure 2-2b) with air (ultra-zero) or Ar (>99.999%) with heating rates varying between 1, 5, and 10°C·min⁻¹. Kinetic studies could not be conducted in the thermogravimetric analyzer mass spectrometer (TGA-MS) due to extreme foaming at hearing rates above 5°C·min⁻¹. Instead, an autotitration system (Figure 2-2a) was used to quantify the HCl(g) released into the off-gas stream. Future tests will be performed to understand the kinetic evolution of HCl(g) and $H_2O(g)$.

The volume of NaOH titrated into the cell was directly used to calculate the amount of HCl(g) that released at each heating rate. The extent of dechlorination, expressed as the conversion (α), was determined by relating the cumulative mass of chlorine removed at a given temperature [$m_{Cl(T)}$] to the theoretical mass of chlorine present in the original sample (m_{Cl}).

$$\alpha(T) = \frac{m_{Cl(T)}}{m_{Cl}} \tag{7}$$

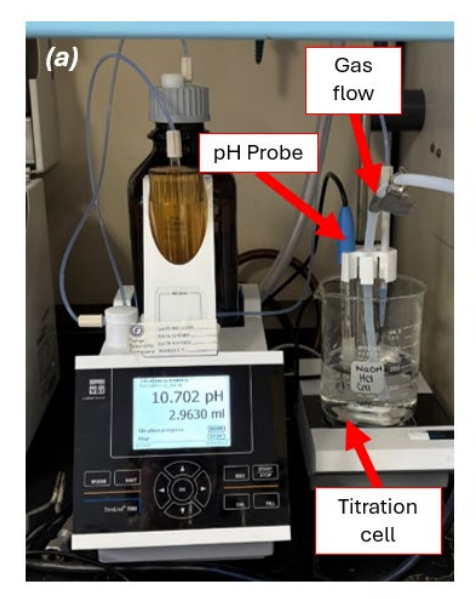




Figure 2-2. (a) The autotitration system (Titroline 7000) connected to the outlet of (b) the tube furnace (MTI Corporation GSL-1600X). In the tube furnace, gas flowed from right to left with any removed byproducts being swept into a Teflon tube, which was inserted into the titration cell shown in (a).

ICP-MS was performed on the dechlorinated product from each test to determine the amount of residual chlorine present in samples after testing and compare these results with the conversion determined by the titration data (Figure 2-7). The residual chlorine for samples processed in air

were found to be greater than those reported in the static testing at a heating rate of 5°C·min¹.(Werth et al. 2025) The lower dechlorination efficacy was likely caused by discrepancies in the actual temperature compared to the furnace set point temperature (Table 2-4), especially at 2 L·min¹, and a greater amount of hydration products remaining in samples processed at 0.1–0.2 L·min¹. Werth et al. determined 300–400°C to be a critical range for the conversion of the aqueous slurry into a polymerized phosphate network. Although the exact relationship between conversion and dechlorination is still unknown, it is known that temperatures lower than 300°C will severely impact dehydration, dehydrochlorination, and condensation reactions.

Table 2-4. Evaluation of the temperature difference (set temperature = 300°C) from the furnace temperature controller (TC1) and an inserted, removable temperature controller (TC2) for 0.1–0.2 L·min⁻¹ and 2 L·min⁻¹ samples in air, highlighting the impact of the flow rate on the final temperature of the furnace.

Time	0.1–0.2 L·	0.1-0.2 L·min ⁻¹ (°C)		า ⁻¹ (°C)
(min)	TC ₁	TC_2	TC ₁	TC_2
1	324	326	322	313
2	319	317	309	296
3	309	301	306	291
4	297	286	292	274
5	317	317	291	271

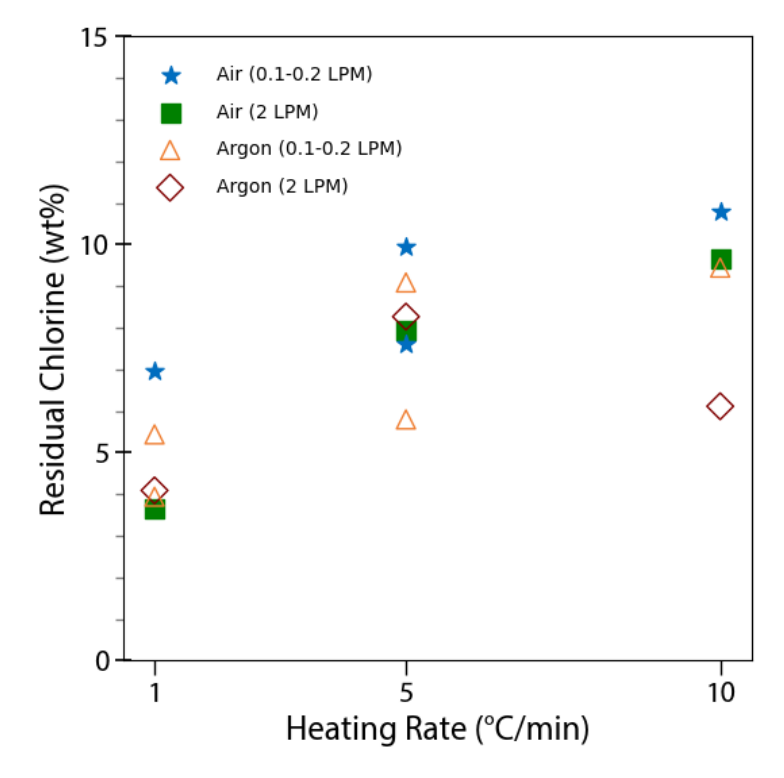


Figure 2-3. Residual chlorine content in the samples with flow rates of 0.1–0.2 L·min⁻¹ and 2 L·min⁻¹ measured with ICP-MS used for kinetics studies as measured by ICP-MS.

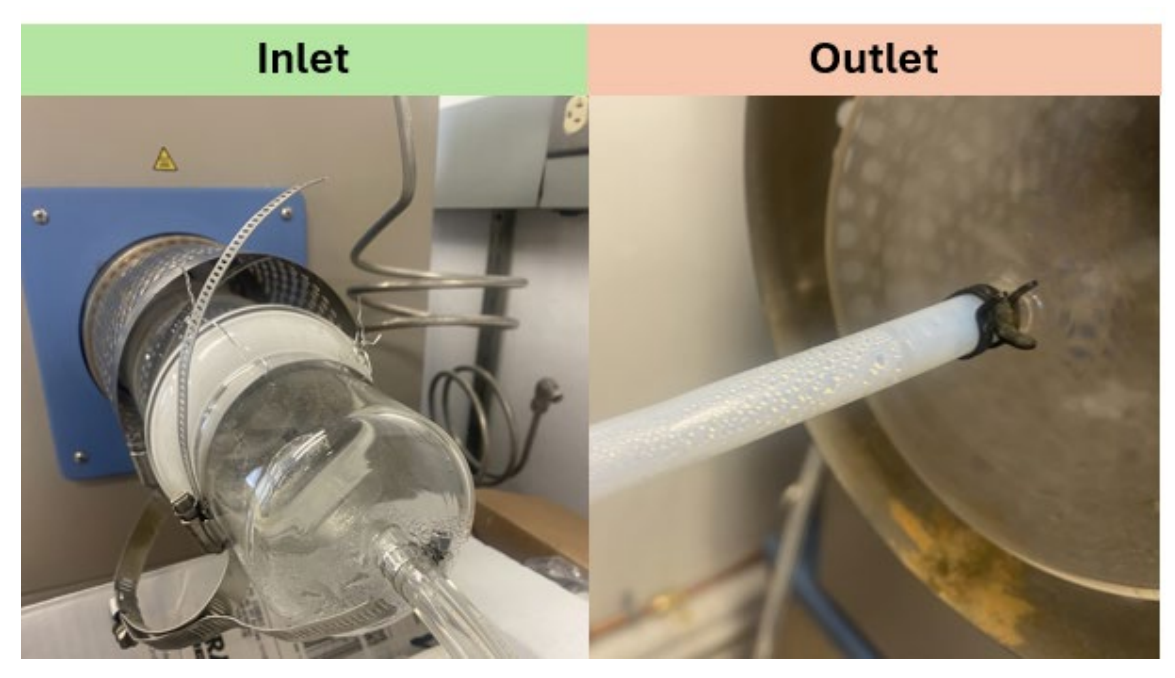


Figure 2-4. Condensation occurring at the inlet and outlet of the tube furnace for attempted kinetic studies with flow rates of 0.1–0.2 L·min⁻¹.

The consumption of 0.1 M NaOH within the autotitrator was used to understand the release of HCl(g) as the heating profile continued (Figure 2-4). (Beland 2025) For heating rates of 1 and 5°C·min⁻¹, the consumption of NaOH(I) was similar for samples processed in either air or argon. For 10°C·min⁻¹, the consumption was greater for the sample processed in argon. (Figure 2-5). Greater dechlorination at slower heating rates was consistent with ICP-MS data, and replicates showed similar HCl(g) release behavior (only 10°C·min⁻¹ is shown in Figure 2-5). Despite the titration data being fairly reproducible, ICP-MS results indicate that the final HCl(g) release values are inaccurate, and thus the reliability of the overall trend remains uncertain. For samples heated in air, the differences were approximately 40, 46, and 55 mass% for samples heated at 1, 5, and 10°C·min⁻¹, respectively, while in argon they were approximately 32, 46, and 53 mass% at the same heating rates. The discrepancy could have been caused by gas entrapment in the transfer lines leading to the titration cell and/or the titrant solution not fully capturing HCl(g) within the setup utilized in the current study.

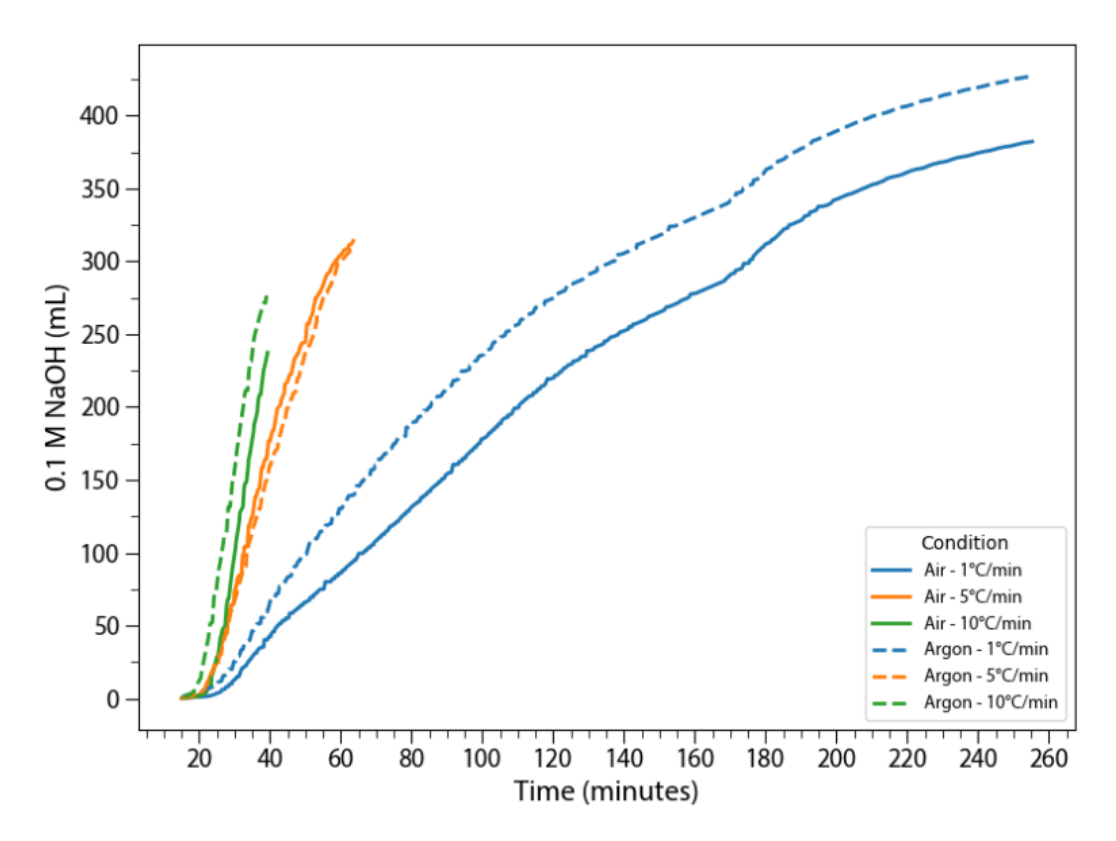


Figure 2-5. NaOH (mL) consumption by off-gassed byproducts during dechlorination of SSM with P/CI = 1 for heating rates of 1, 5, and 10°C·min⁻¹ in air (solid lines) and argon (dashed lines) at 2 L·min⁻¹.

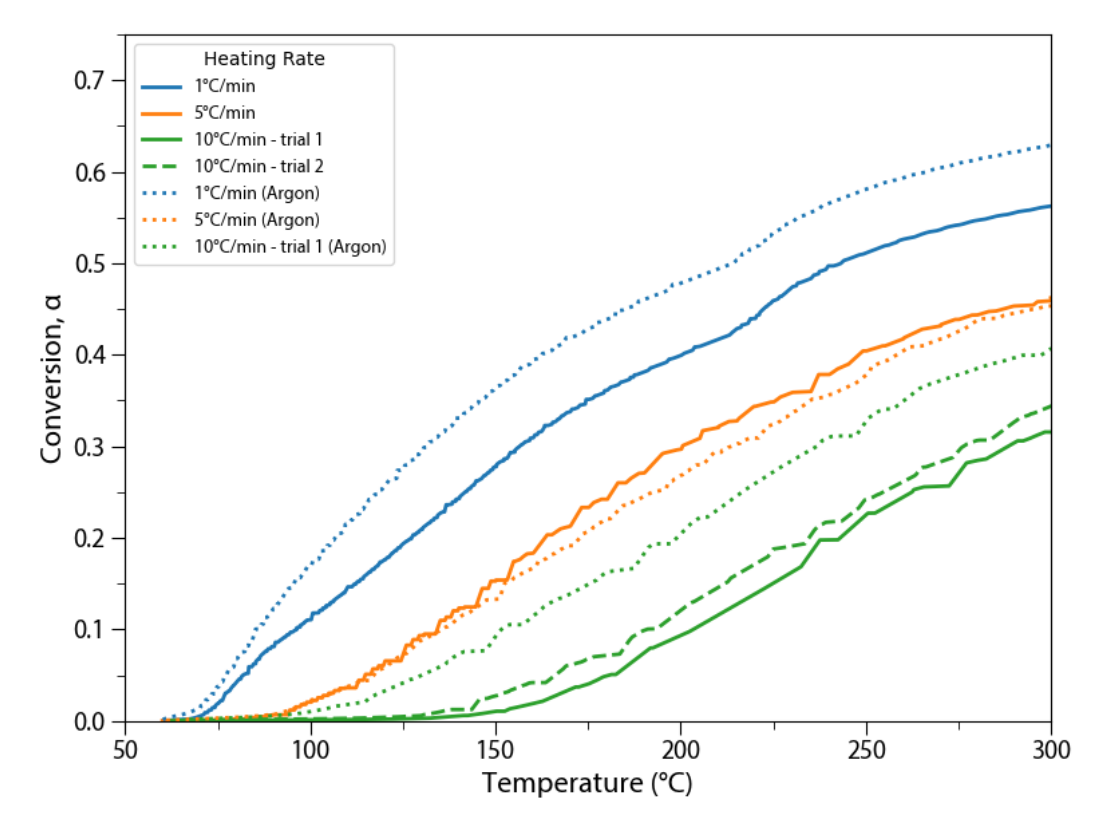


Figure 2-6. Conversion of CI resulting from dechlorination of at 1, 5, and 10°C·min⁻¹ heating rates in air (solid lines) or argon (dotted lines) and gas flow rate of 2 L·min⁻¹. Conversion was greatest for samples processed in argon with heating rates of 1°C·min⁻¹. Repeated trials for some samples are shown.

The concurrent release of HCl(g) and $H_2O(g)$ led to complex, temperature-dependent, multi-step reactions that complicate assignment of a single kinetic model. Therefore, an isoconversional Kissinger-Akahira-Sunose (KAS) method was employed, as this model-free approach enables determination of activation energy (E_a) as a function of both temperature and conversion (Vyazovkin and Wight 1999; Tarani and Chrissafis 2024).

For this study, the value of E_a was evaluated at each conversion level for all heating rates using Eqn. (8) where β_i is the heating rate, $T_{a,i}$ is absolute temperature, R is the universal gas constant, and T is the temperature (Tarani and Chrissafis 2024). E_a was determined for two regions, including 100–200°C and 200–300°C.

$$\ln\left(\frac{\beta_i}{T_{\alpha,i}^2}\right) = Const. - \frac{E_{\alpha}}{RT} \tag{8}$$

Despite the overall similarity of the conversion profiles for samples processed in air and argon (Figure 2-5a and Figure 2-5b), small differences in slope, especially at 1°C·min⁻¹, resulted in strongly contrasting activation energy trends (Figure 2-6a and Figure 2-6b). Due to gas-capture limitations, the following analysis should be considered preliminary, and additional testing with improved gas capture is required to more accurately resolve the temperature dependence of E_a.

Examination of E_a in air and argon environments revealed important differences in the chlorine removal from the melt (Figure 2-6a and Figure 2-6b). In argon, E_a was initially high but decreased steadily with conversion, suggesting that additional reaction pathways become available for chlorine volatilization as conversion progresses. In contrast, in air, E_a remained fairly constant between $100-200\,^{\circ}\text{C}$, implying that a dominant mechanism facilitates chlorine removal in this region likely aided by $O_2(g)$ at the melt surface and resulting in lower initial E_a values. This behavior changes in the $200-300\,^{\circ}\text{C}$ region, where E_a rises sharply, consistent with a transition to a less favorable mechanism. A possible explanation is that $O_2(g)$ no longer contributes to dechlorination at elevated temperatures, leading to either a change in the reaction interface or accumulation of oxidation products on the melt surface.

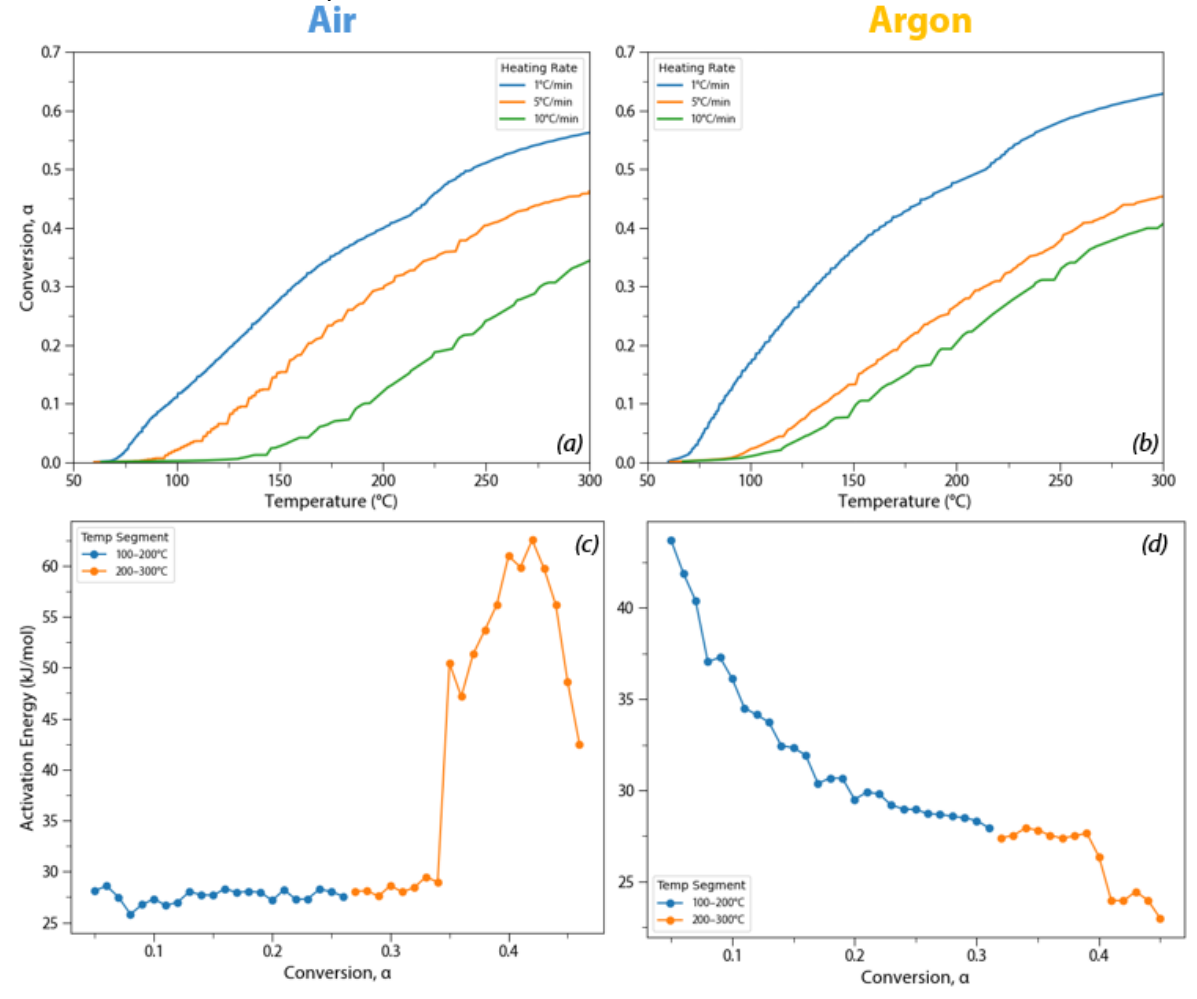


Figure 2-7. Chlorine conversion analyzed using the KAS method for (a) air and (b) argon environments. *E*_a was derived from the conversion profiles in the 100–200°C and 200–300°C temperature ranges for (c) air and (d) argon.

3.0 Evaluation of Potential Crucibles Materials

The highly corrosive nature of phosphate melts during dechlorination and vitrification necessitates an investigation into compatibility with the types of available containment materials. At this time, it is still unknown if the waste will undergo continuous or batch processing. For a continuous process (see Figure 3-1 for an example), dechlorination could be performed in a rotary kiln with ports to allow for off-gas release as waste is poured into a melter. In the melter, a port could be added to enable charging the dechlorinated product with additives into the hot zone for producing the final waste form. For a batch process (see Figure 3-1 for an example), it would be desirable to not have to cool between dechlorination and vitrification steps, or change the crucible (melt containment) between these steps. Although more complex than a batch process, a continuous process could mitigate some issues related to the two-step process, such as charging the batch with additives at high temperatures if the crucible is unable to withstand the thermal shock from cooling after dechlorination. However, if raw materials could be replaced with a glass frit or compositional adjustments could enable single-step processing, batch processing might be a more suitable option than a continuous processing system.

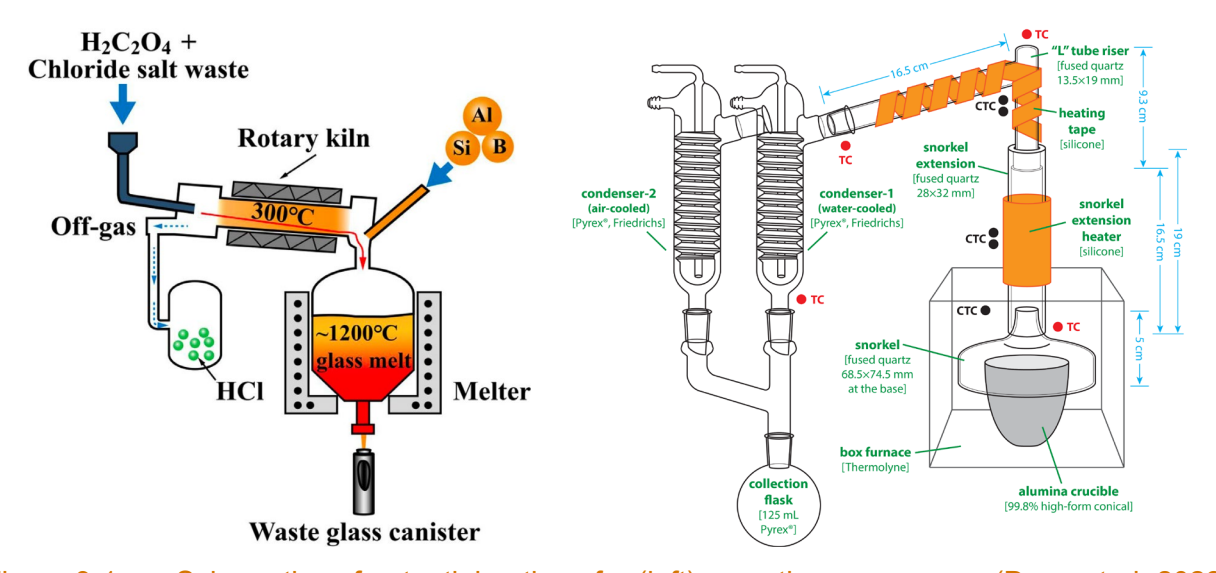


Figure 3-1. Schematics of potential options for (left) a continuous process (Dong et al. 2022) and (right) a batch process (Riley et al. 2020) for salt waste treatment.

Silica and alumina crucibles were initially selected for dechlorination due to availability, cost, and for comparison with a previous study by Riley et al. (2020). After issues with alumina cracking and leaking during dechlorination and subsequent vitrification, testing was conducted only in silica. As discussed above, no crucible fracture was observed for SSM processed $\leq 400^{\circ}$ C but fractures were observed in $\approx 50\%$ of cases at $500-600^{\circ}$ C.

Extended holds were used to examine incorporation of Si into the phosphate melt during dechlorination due to silica crucible degradation. These tests revealed increased Si contamination (Figure 3-2a), with ~0.4 mass% more Si detected in the 600°C samples compared with the 400°C samples after 12 h isothermal holds. Additional data are being collected to determine the solubility limit and its structural effects. Interestingly, after 12 h isothermal holds, crucibles processed at 400°C fractured, while those processed at 600°C did not (Figure 3-2b). Additional testing is needed to clarify crucible degradation rates during dechlorination using different precursor materials.

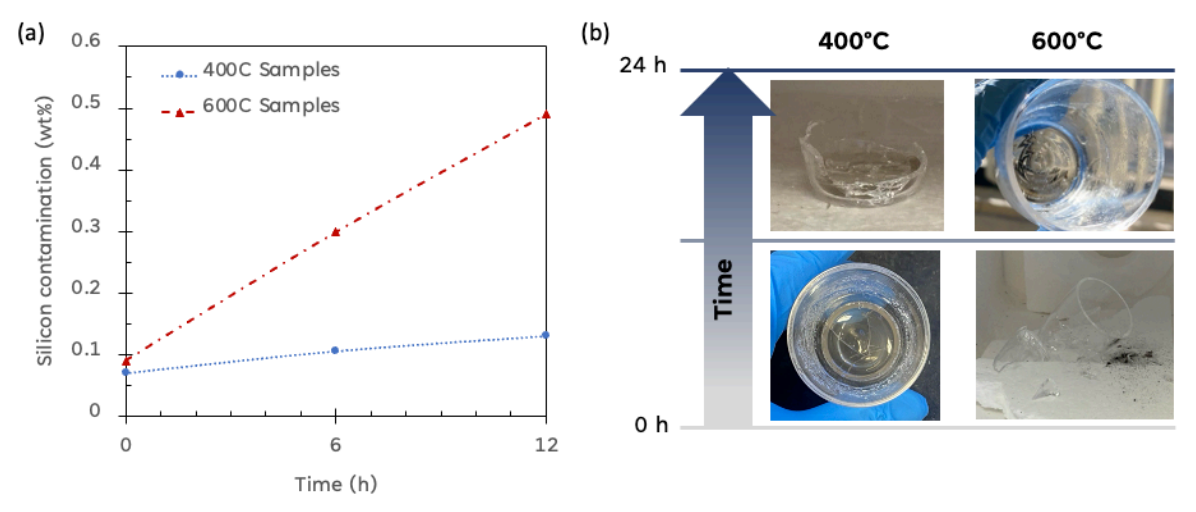


Figure 3-2. (a) Silicon contamination as a function of hold time for samples processed in silica crucibles at 400°C and 600°C. (b) Photographs of crucibles after 0 h and 24 h dwells at 400°C and 600°C.

Interactions between iron phosphate melts and various crucible materials were examined: fused quartz (GM Quartz), alumina (AdValue, AL-P-102-76-6), SS316L, Inconel 693 (Special Metals, UNS N06693), and Monofrax K-3 (shown in Figure 3-3). The iron phosphate glass was made by Mo-Sci Corporation using two different precursors, ADP or H₃PO₄ (Table 3-1). Because only 500 g of glass was available from each precursor, the frits were combined for testing. For each test, 35 g of the frit mixture was added to a 50 mL silica crucible (AdValue, high form, FQ-1050).

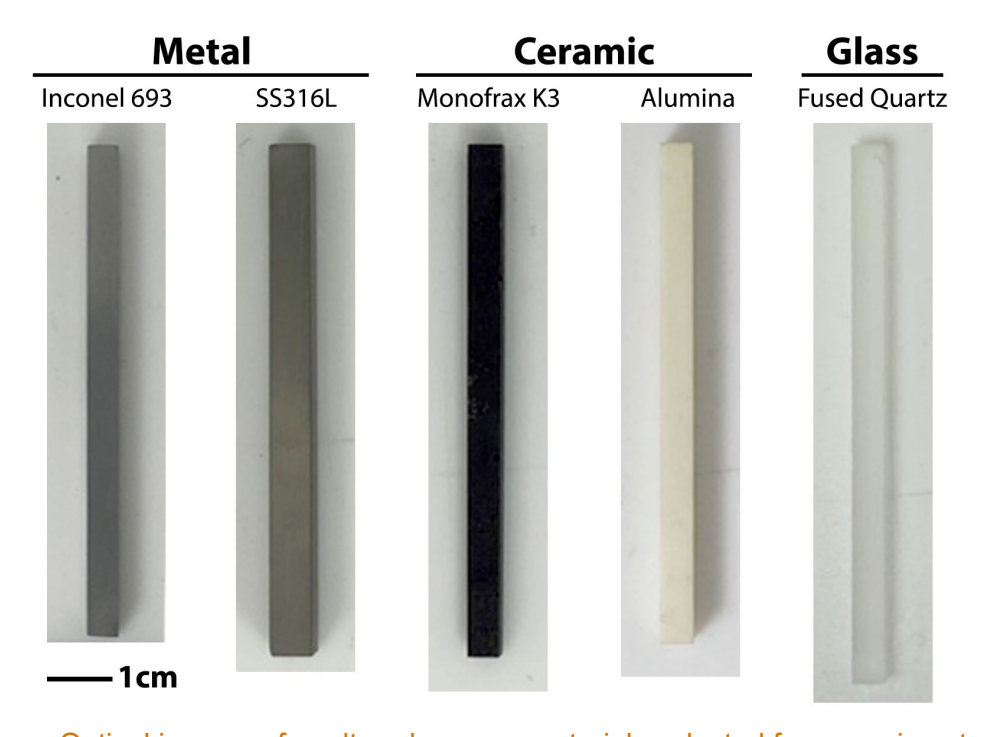


Figure 3-3. Optical images of unaltered coupon materials selected for corrosion study.

Table 3-1. Composition of the binary iron phosphate glass frit produced by Mo-Sci Corporation for corrosion studies.

Oxide	Mole%
P ₂ O ₅	39.85
Fe ₂ O ₃	26.10
Li ₂ O	16.36
K ₂ O	11.35
Na2O	3.33
Cs ₂ O	0.90
SrO	0.81
CeO ₂	0.88
$Nd_2O_3\\$	0.42
SUM	100.00

Each bar was secured to the center of a refractory lid with 907 GF Smooth Fine Grade Putty to suspend the bar in the molten glass as shown in Figure 3-4. For the alumina and fused quartz bars, the cement was either allowed to cure without heat treatment or was heat-treated according to manufacturer instructions. Samples with heated-treated cement were allowed to cool for up to 12 h before testing. For metal samples, the cement was allowed to cure without heat treatment according to manufacturer instructions. The bars were immersed in glass frit and heated under air or argon (ultra-high purity, >99.999%) to 1050°C and held at that temperature for 1 h or 4 h. Bars were removed from the molten glass and cooled in air after the testing period. Corroded bars were longitudinally cross-sectioned and polished with water-free procedures on the cut surface for scanning electron microscopy (SEM) and energy dispersive X-ray spectroscopy (EDS) analyses. Key regions of the sample are noted in Figure 3-4c. Corrosion of the bar at the melt line may result in a neck region and molten glass may interact with the sample above the neck region.

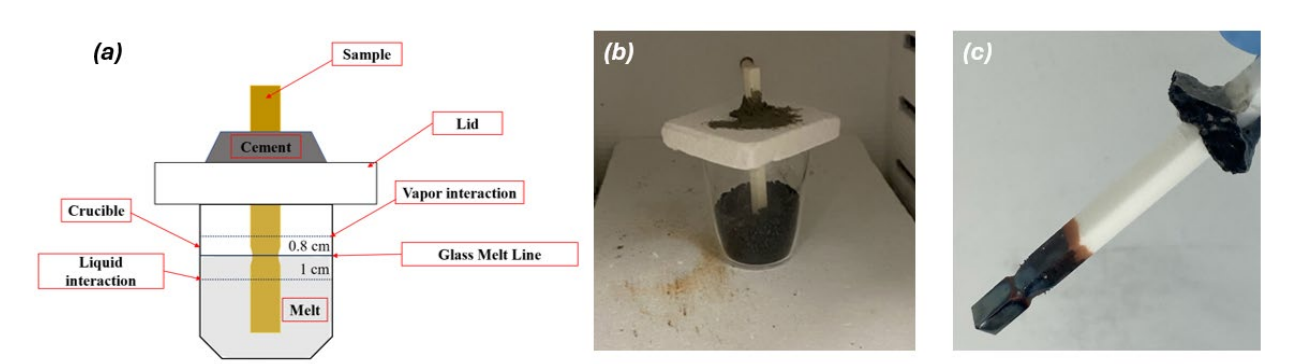
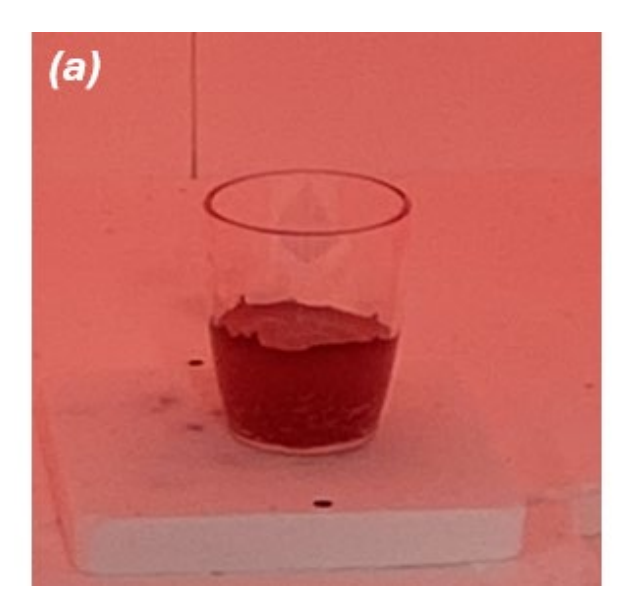


Figure 3-4. (a) A schematic of crucible-melt interaction, (b) the experimental setup before testing, and (c) the bar shown after removal from the melt (alumina bar is shown).

Foaming was observed during heating of the frit (Figure 3-5). The foaming is suspected to be caused by the release of water as a result of water-quenching during frit synthesis. It was unknown to the team that water quenching was performed by Mo-Sci until after initial tests with the glass.



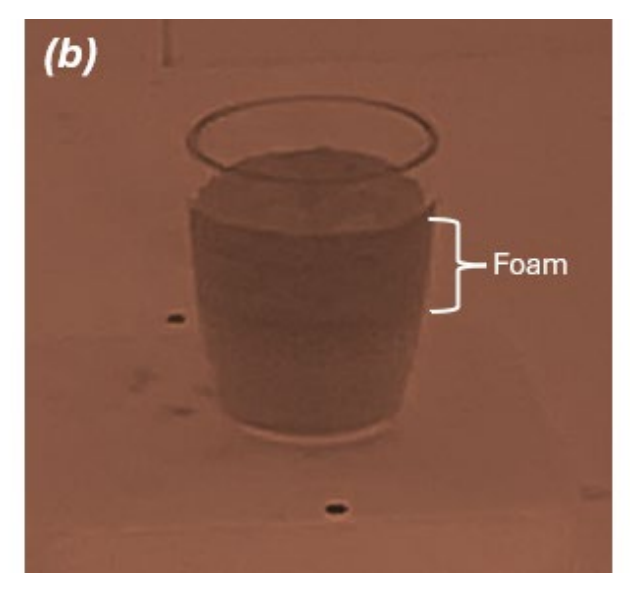


Figure 3-5. Pictures of (a) the initial melting of Mo-Sci frit and (b) the foaming that occurred after reaching the glass transition temperature (T_g). Image (b) was color corrected for better visualization. For scale, these crucibles are 53 mm in height (see additional dimensions listed previously).

Table 3-2 summarizes the performance of each material and the corresponding test conditions. The corroded area of the neck was measured in the 10.8 mm section of the bar near the melt meniscus. The sections following Table 3-2 are in the order of ranking from the best performer (fused quartz) to worst performer (Inconel 693).

Table 3-2. Summary of corrosion of bars in molten DPF5-336. The corroded area was determined by OM in the 13.8 mm region around the neck. Oxide depth, penetration depth, and crack depth were determined with SEM-EDS. Penetration depth includes the oxide depth. N/A = not applicable, with footnotes below the table with additional details. ID = identification.

Coupon Material	Atmos.	Test Time (h)	Sample ID	Corroded Area at the Neck (mm²)	Oxide Depth (µm)	Maximum Penetration Depth (µm)	Crack Depth (µm)	Secondary Phases	Ranking
	Air	1	Fused quartz- Air-1h	N/A ^(a)	N/A ^(b)	150 ^(c)	<220 ^(d)		
Fused quartz	All	4	Fused quartz - Air-4h	N/A ^(a)	N/A ^(b)	200 ^(c)	<300 ^(d)	N/A ^(e)	1
ruseu quanz	Armon	1	Fused quartz - Ar-1h	N/A ^(a)	N/A ^(b)	200 ^(c)	<240 ^(d)	IN/A ⁽⁻⁾	
	Argon	4	Fused quartz - Ar-4h	N/A ^(a)	N/A ^(b)	200 ^(c)	<300 ^(d)		
	Air	1	Alumina-Air-1h	0.96	<5	N/A ^(f)	N/A ^(g)		
Alumina	All	4	Alumina-Air-4h	N/A ⁽ⁱ⁾	<5	N/A ^(f)	N/A ^(g)	Iron oxide ^(h)	2
Alumina	Argon	1	Alumina-Ar-1h	1.70	<10	N/A ^(f)	N/A ^(g)		
		4	Alumina-Ar-1h	3.71	<20	N/A ^(f)	N/A ^(g)		
	Air	1	K3-Air-1h	0.41	30-50	250	N/A ^(g)	Chromium oxide ^(j)	3
M 6 160		4	K3-Air-4h	3.62	<100	2500	N/A ^(g)		
Monofrax K3	Argon	1	K3-Ar-1h	0.37	30-50	180	N/A ^(g)		
		4	K3-Ar-4h	2.03	10-60	520	N/A ^(g)		
	Δ:	1	SS-Air-1h	8.90	>1000	1300	N/A ^(g)		
SS316L	Air	4	SS-Air-4h	N/A ^(h)	N/A ^(h)	N/A ^(h)	N/A ^(h)	Chromium oxide, Mo,	
55310L	A	1	SS-Ar-1h	14.20	<100	500	N/A ^(g)	Ni, P, Fe alloy ^(k)	4
	Argon	4	SS-Ar-4h	N/A ^(h)	N/A ^(h)	N/A ^(h)	N/A ^(h)	,	
Inconel 693	Air	1	Inconel-Air-1h	N/A ⁽ⁱ⁾	>1000	100	N/A ^(g)	Cr and Al oxides, Ni	5
Inconel 693	Argon	1	Inconel-Ar-1h	28.34	>1000	100	N/A ^(g)	and P alloy ^(k)	

(a)The material loss at the neck region of fused quartz samples could not be determined with optical microscopy due to a combination of surface cracking, DPF5-336 deposits, and lack of a distinct sample edge due to the optical clarity of the material; however, material loss due to degradation appeared to be negligible (see Figure 3-6, Figure 3-7, Figure 3-8, and Figure 3-9). (b)No oxide layer was observed in fused quartz samples. (c)Maximum penetration depth in fused quartz bars occurred in cracks. (d)Cracks were approximately equal in depth over the entire surface of the fused quartz bar exposed to DPF5-336. (e)Fused quartz bars did not have secondary phases composed of corroded material. (f)Penetration of DPF5-336 components into the bulk of alumina bars was not observed. (g)Sample did not have cracks. (h)The iron oxide layer was homogeneous in both composition and thickness over the surface of the bar. (i)The area corroded in the neck region could not be determined due to the extensive material loss in this sample that caused the sample to separate into two sections during preparation. (i)Chromium oxide and DPF5-336 formed a heterogeneous layer that varied in thickness over the surface of the bar. (k)Secondary phases formed a heterogeneous corroded layer that varied greatly both in composition and thickness depending on the location on the bar.

3.1 Fused quartz

Surface cracking upon cooling was observed in fuzed quartz bars degraded by the molten DPF5-336. Sections of the sample surface separated during preparation because of the extensive surface cracking, which are shown in Figure 3-6, Figure 3-7, Figure 3-8, and Figure 3-9. Due to the cracking and flaking of the bar surface, only a small portion of the surface of the fused quartz bar corroded in argon for 4 h remained intact for analysis as shown in Figure 3-9a. For these tests, the molten DPF5-336 penetrated into the bar along transverse cracks that originate at the interface between the bar and the DPF5-336. The fused quartz bars degraded over the entire surface exposed to the molten DPF5-336.

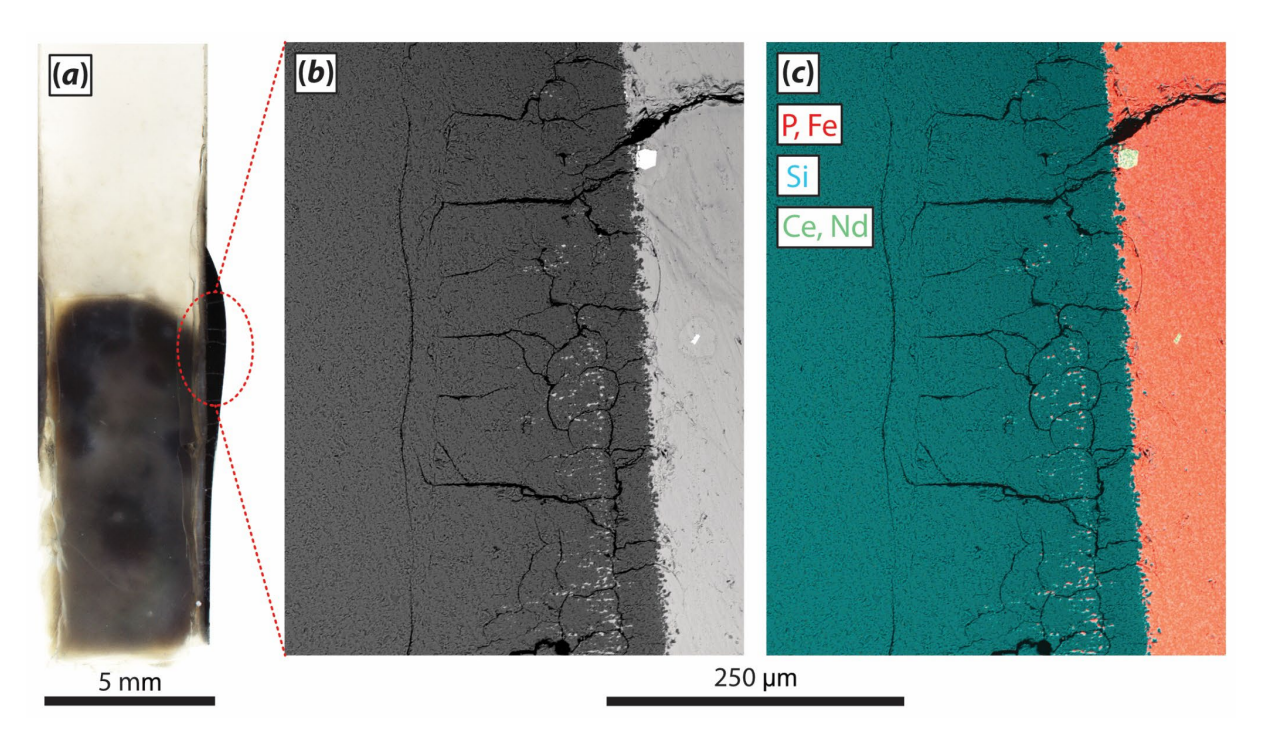


Figure 3-6. The fused quartz-Air-1h sample is shown. The optical image in (a) shows the portion of the fused quartz bar that was in contact with the molten DPF5-336. A BSE image of the bar edge (b) and corresponding EDS map (c) in the meniscus region shows DPF5-336 penetration and transverse cracks.

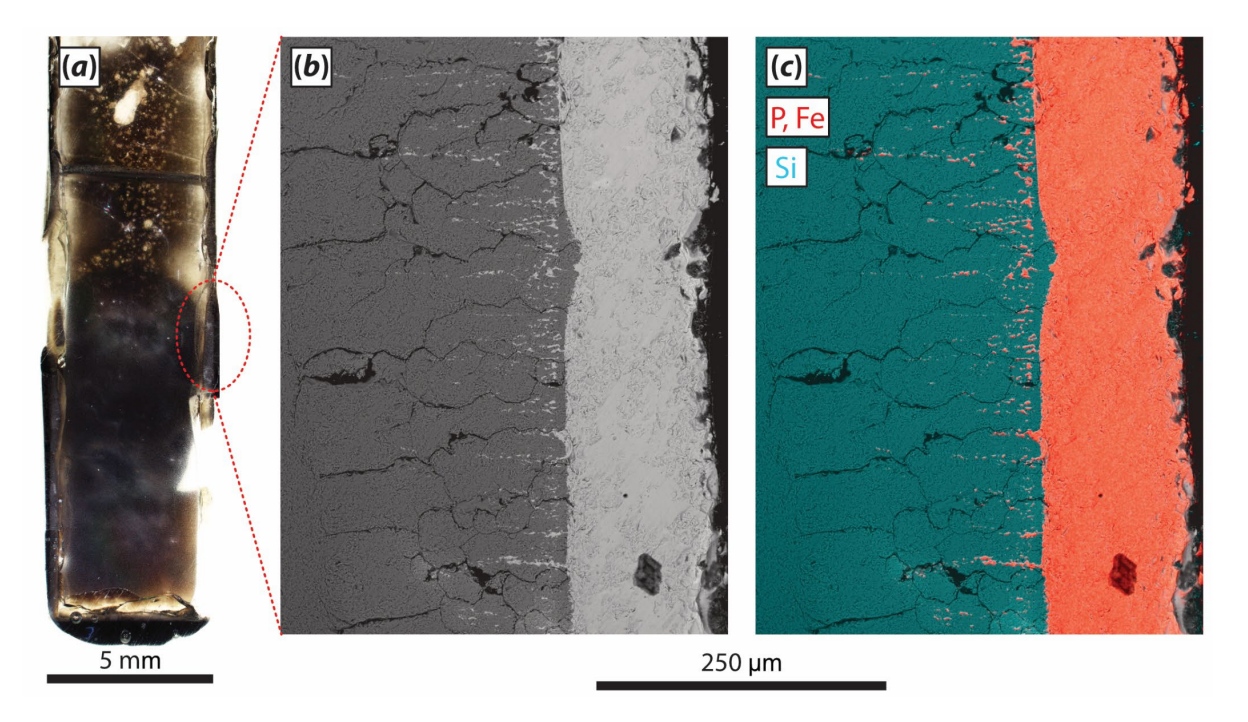


Figure 3-7. The fused quartz-Ar-1h sample is shown. The optical image in (a) shows the portion of the fused quartz bar that was in contact with the molten DPF5-336. A BSE image of the bar edge (b) and corresponding EDS map (c) in the meniscus region shows DPF5-336 penetration and transverse cracks.

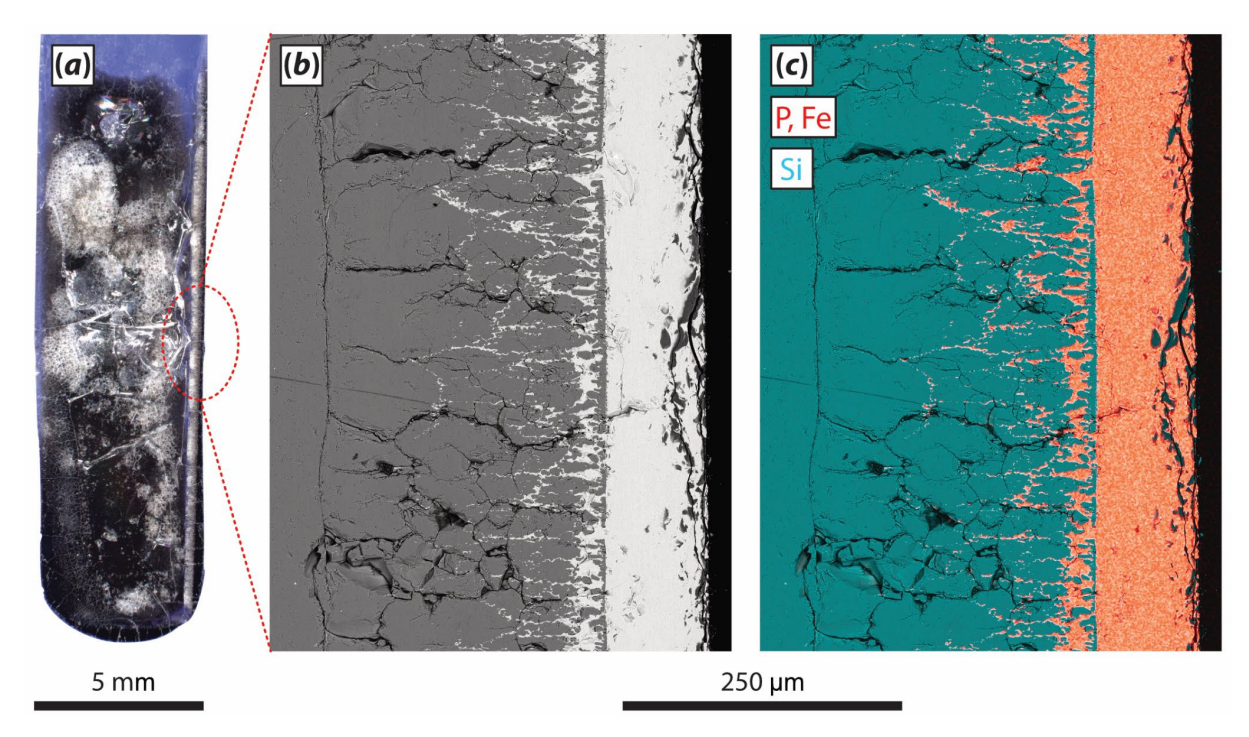


Figure 3-8. The fused quartz-Air-4h sample is shown. The optical image in (a) shows the portion of the fused quartz bar that was in contact with the molten DPF5-336. A BSE image of the bar edge (b) and corresponding EDS map (c) in the meniscus region shows DPF5-336 penetration and transverse cracks. The blue color in (a) is from the type of epoxy used to mount the sample prior to cutting and polishing.

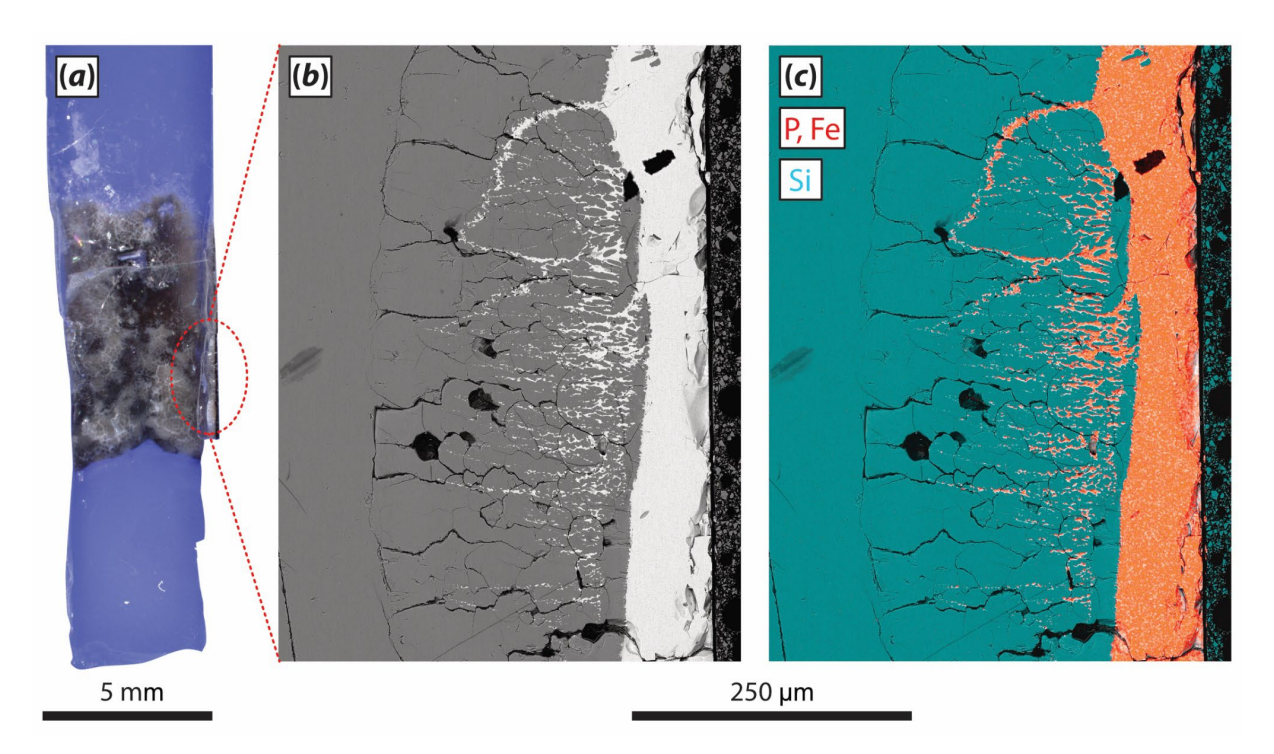


Figure 3-9. The fused quartz-Ar-4h sample is shown. The optical image in (a) shows the portion of the fused quartz bar that was in contact with the molten DPF5-336. A BSE image of the bar edge (b) and corresponding EDS map (c) in the meniscus region shows DPF5-336 penetration and transverse cracks. The blue color in (a) is from the type of epoxy used to mount the sample prior to cutting and polishing.

3.2 Alumina

Alumina bars in all testing conditions exhibited resistance to the penetration of the molten DPF5-335 into the bulk of the bar (Figure 3-10, Figure 3-11, Figure 3-12, and Figure 3-13). The greatest degradation of the bar occurred at the glass melt line. After 1 hr, the sample corroded in an air atmosphere lost <1.0 mm² of material at the meniscus region compared to ≈ 1.70 mm² for the Ar sample. However, after 4 hrs, the melt had extensively corroded the air sample while the Ar sample remained intact. An iron oxide layer (presumably Fe₂O₃) formed along the edge of all bars, which has been documented in previous studies by members of this team (Riley et al. 2023).* The layer was typically thinner (often <1 µm) at the melt line (meniscus) region and thicker in the completely submerged region below the location of the melt line (see Figure 3-4a for a description of these locations). In the air samples, the greatest thickness of the layer was 5 µm. The greatest thickness of the iron oxide layer in the 1-h and 4-h Ar samples was 10 µm and 20 µm, respectively. Therefore, it appears that longer testing periods and an Ar atmosphere favor the formation of the iron oxide layer at the edge of the alumina bar. Other products of the corrosion test include separated phases in the residual DPF5-336. Two types of dendrites were observed in the residual DPF5-336. The concentration of selected components in the dendrites and matrix phase, as measured by EDS, are shown in Table 3-3. Dendrites present in the residual DPF5-335 at the meniscus region in air samples and in both the meniscus and submerged region of the 4 h sample run in argon appear to be a crystalline iron phosphate phase with a similar composition to the

^{*} The formation of the Fe₂O₃ layer could be caused by an insolubility/precipitation phenomenon or through a nucleation/growth reaction where the coupon was in contact with the melt.

surrounding material. It is possible that there is a difference in Li concentration that cannot be measured by this method. The argon 4 h sample additionally contained darker dendrites with a higher Al concentration than the surrounding material, indicating the formation of an aluminum iron phosphate phase. Also, the bright phase in Figure 3-12c is a Ce, Nd, P, O phase that is presumed to be monazite was detected in the residual DPF5-336 in the meniscus region of the 4 h sample run in air.

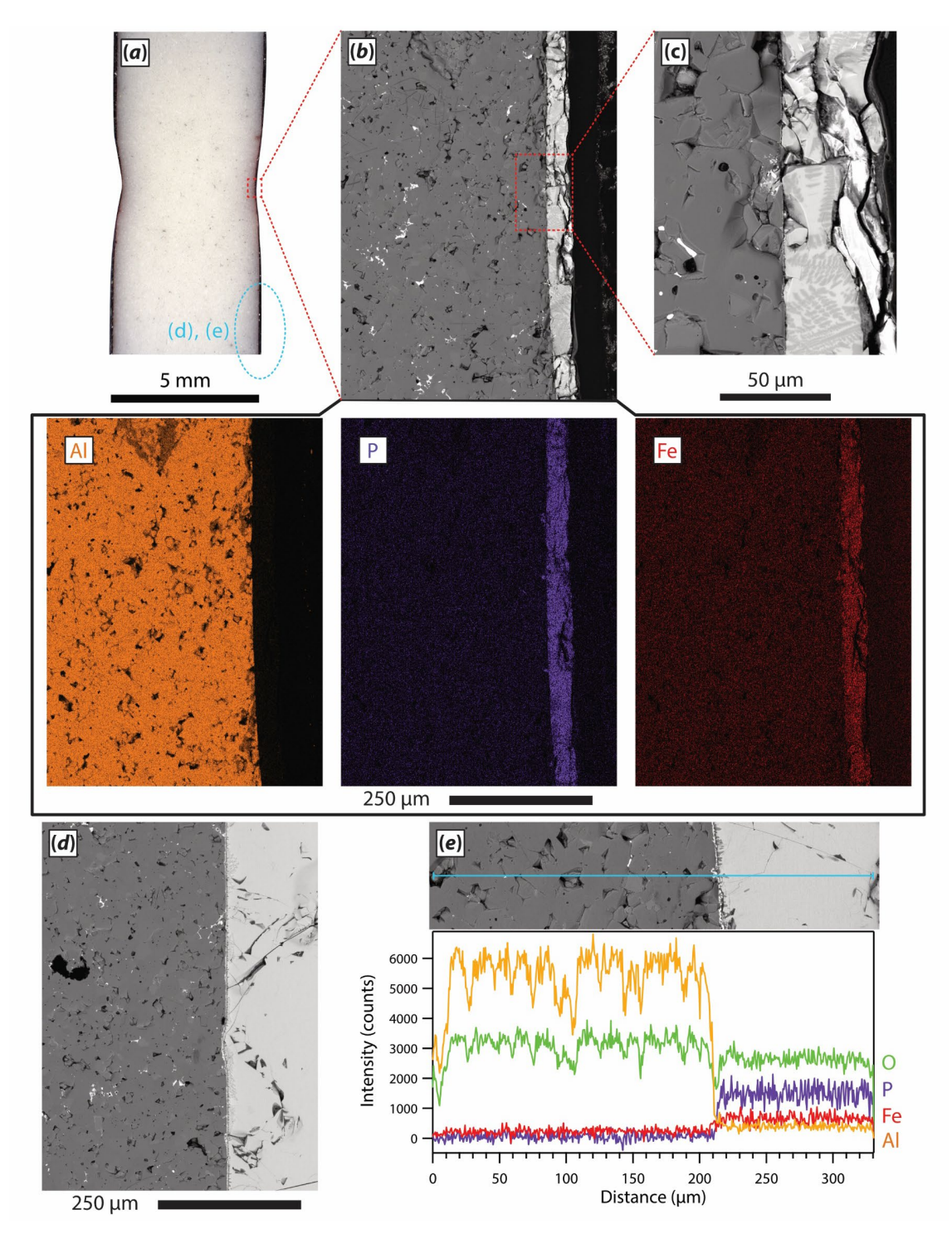


Figure 3-10. The Alumina-Air-1h sample is shown. The optical image in (a) shows a slight divot in either side of the bar at the melt meniscus. The BSE image and EDS maps in (b) reveal the distinct edge between the alumina bar and the residual DPF5-336 at the melt meniscus. An inset dashed box indicates a region shown in (c), showing dendrites in the residual DPF5-336. Images from the portion of the bar completely submerged in (d) and (e) and the linescan in (e) confirm the exclusion of the DPF5-336 from the alumina bar.

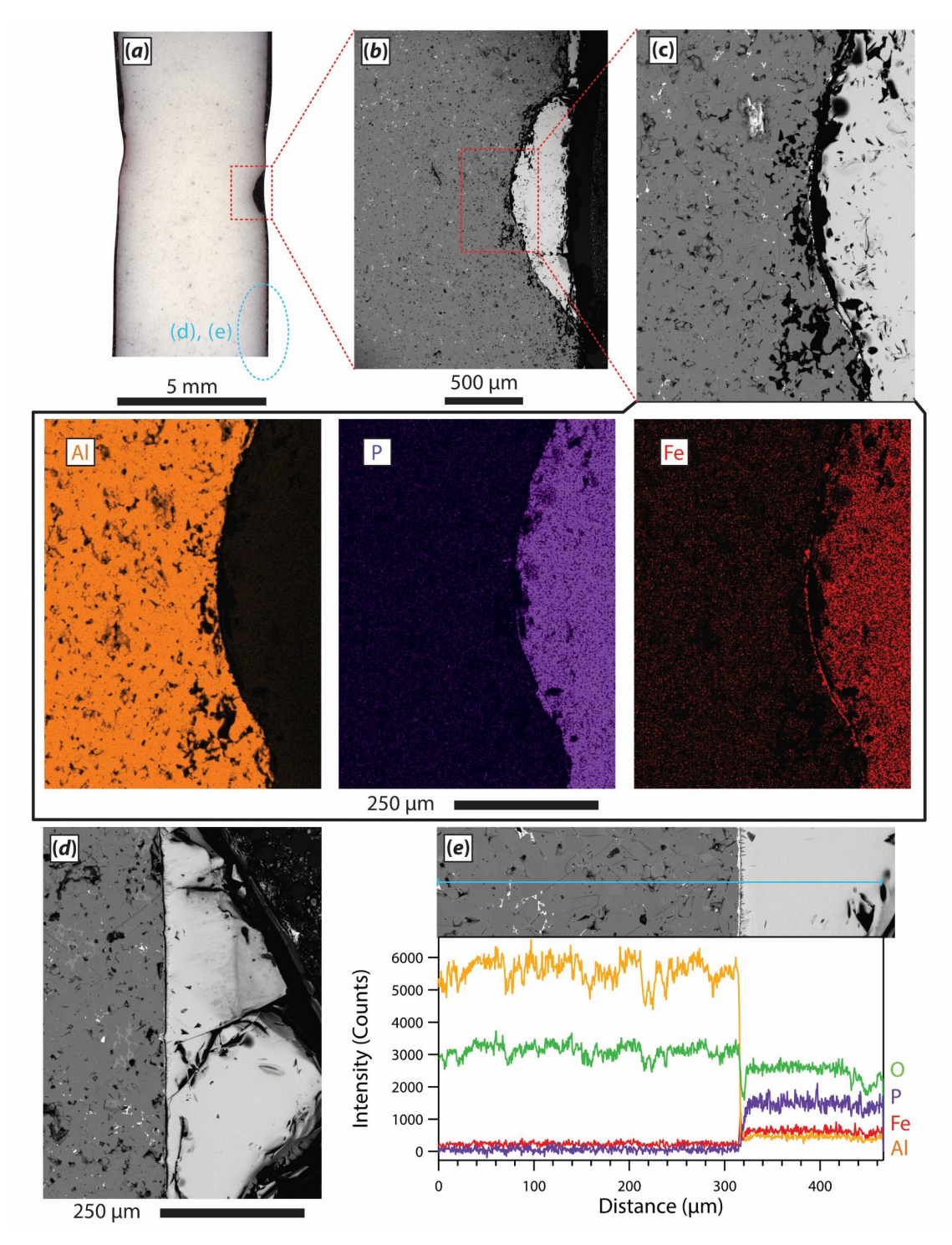


Figure 3-11. The Alumina-Ar-1h sample is shown. The optical image in (a) shows divots in the bar at the meniscus of the melt. A large divot was investigated with SEM/EDS as shown in (b) and (c), revealing an iron-rich layer between the alumina bar and the residual DPF5-336. BSE Images from the portion of the bar completely submerged in the melt are shown in (d) and (e). The linescan in (e) shows an increased concentration in iron in the layer between the alumina bar and the DPF5-336.

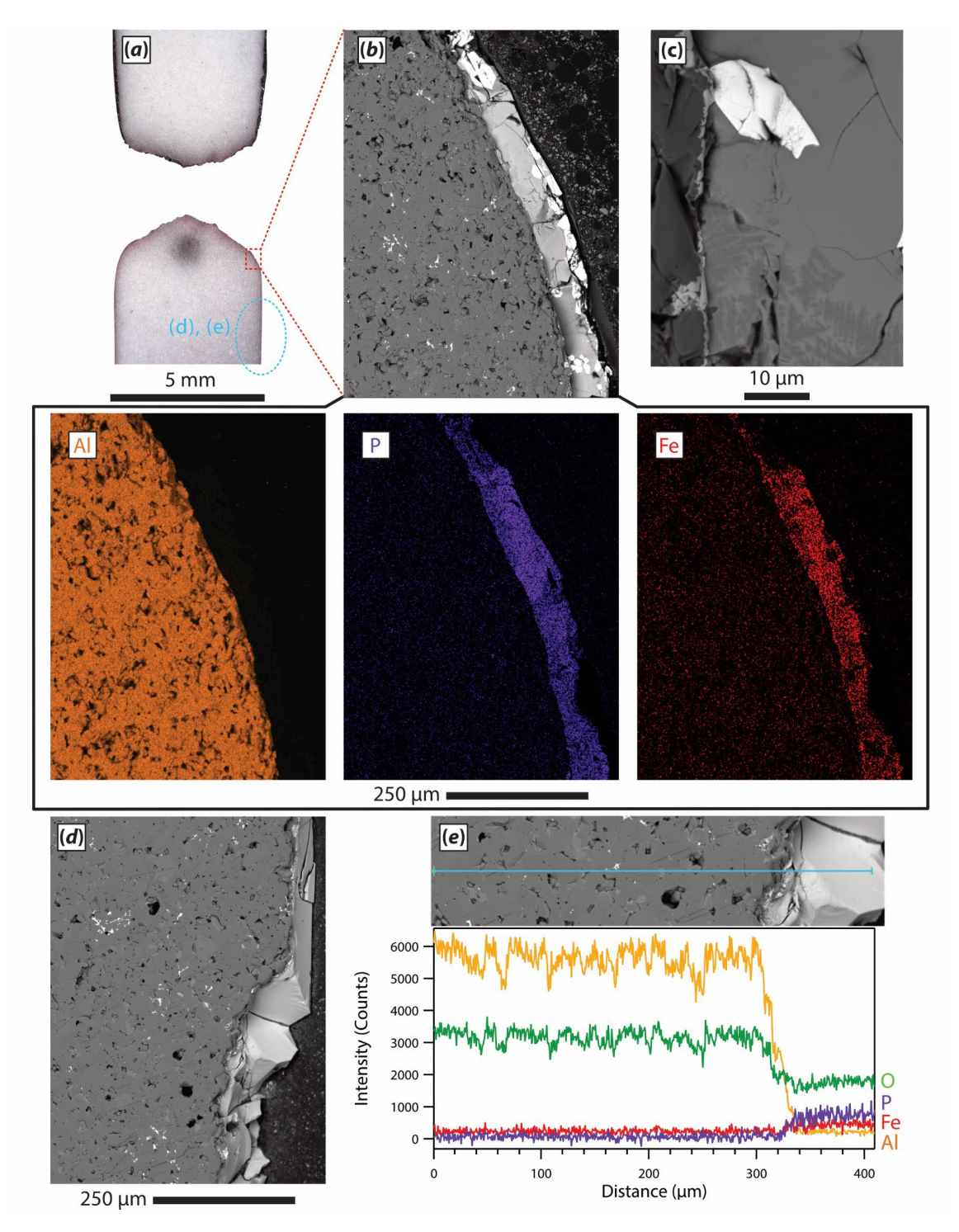


Figure 3-12. The Alumina-Air-4h sample is shown. The image in (a) of the region of the bar at the melt meniscus shows that the bar has separated into two pieces during sample prep. SEM/EDS images in (b) show the distinct edge between the alumina bar and the residual DPF5-336 near the melt meniscus. The bright phase in the residual DPF5-336 is shown in greater detail in (c). Images from the portion of the bar completely submerged in (d) and (e) and the linescan in (e) confirm the exclusion of the DPF5-336 from the alumina bar.

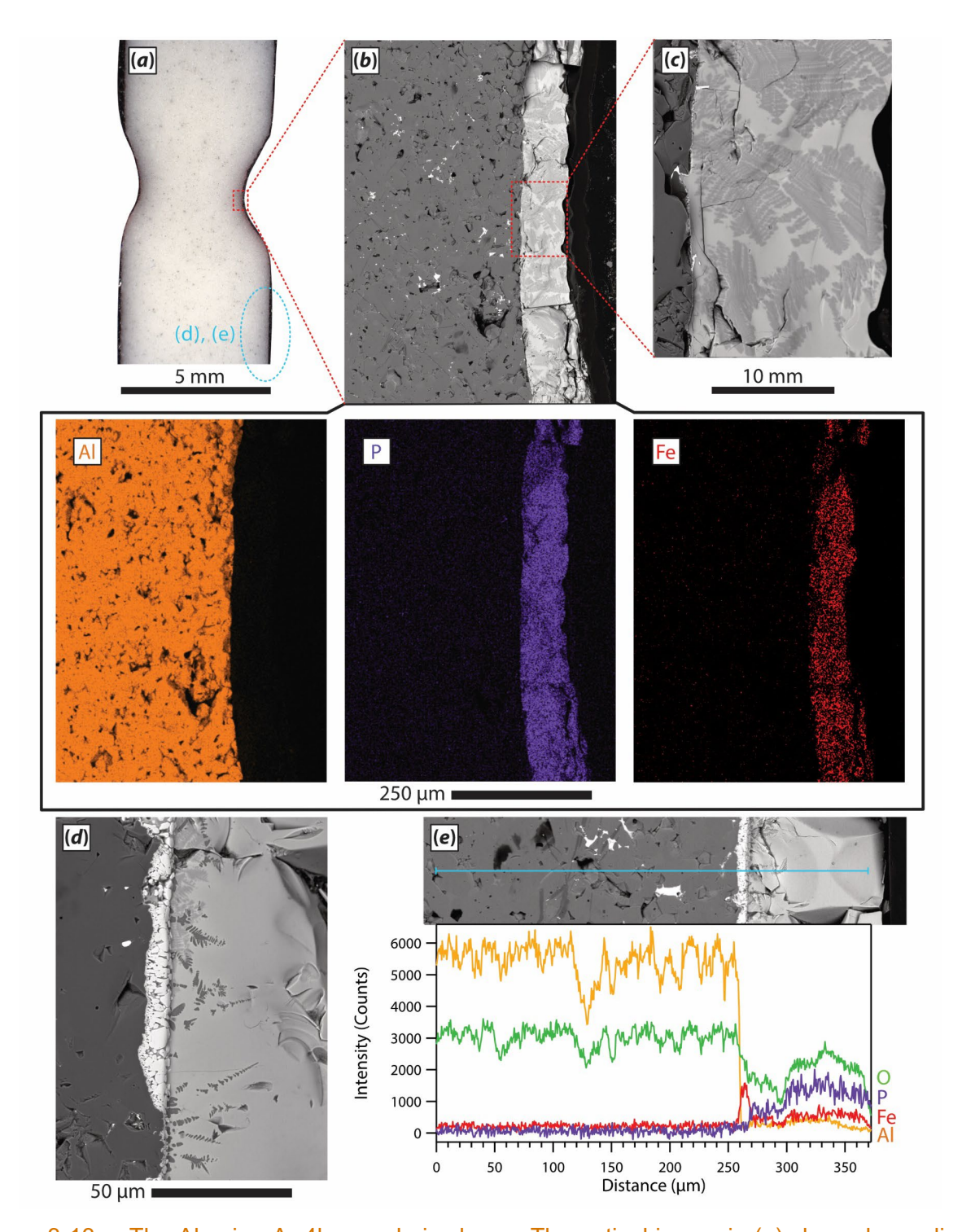


Figure 3-13. The Alumina-Ar-4h sample is shown. The optical image in (a) shows large divots in the bar at the meniscus of the melt. A divot was investigated with SEM/EDS as shown in (b) revealing the distinct edge between the bar and the residual DPF5-336. A closer view of that edge in the divot region in (c) shows extensive formation of dendrites in the residual DPF5-336. The BSE image in (d) from the portion of the bar completely submerged in the melt shows two types of dendrites formed in the residual DPF5-336 along with bright layer at the sample edge. The linescan in (e) shows an increased concentration in iron in the edge layer.

Table 3-3. Concentration of selected elements in different regions of the residual DPF5-336 in the Alumina-Ar-4h sample as measured by EDS (Figure 3-13d).

Element	Dark Dendrites		Light Dendrites		Matrix	
	Mass%	Error	Mass%	Error	Mass%	Error
Al	18.20	0.26	2.89	0.14	4.18	0.11
Р	22.94	0.38	19.86	0.60	17.78	0.37
Fe	8.20	0.49	25.46	1.08	24.21	0.71
Na	0.03	0.05	0.78	0.11	1.08	0.08
K	0.44	0.08	4.54	0.23	7.80	0.19
Cs	-	-	-	-	3.39	0.38

3.3 Monofrax K-3

Like the alumina bars, the Monofrax K-3 bars exhibited the greatest loss of material in the meniscus region of the molten DPF5-336. Material loss from neck region was < 1 mm² in either atmosphere. Greater material losses of 3.6 and 2.0 mm² occurred after 4 h in air and argon. respectively. Although material loss at the neck was limited, components from the DPF5-336 penetrated along the boundary of Al-rich and Mg-rich phases, as shown in Figure 3-14, Figure 3-15. Figure 3-17, and Figure 3-18. For samples at the same test duration, the depth of penetration was greater in samples corroded in air compared to argon. Penetration depth was greatest in the sample corroded in air for 4 h with regions at the neck (Figure 3-15) and in the submerged region (Figure 3-16) with glass components detected up to 2.5 mm from the surface of the bar. A chromium oxide corrosion layer up to 100 µm thick was interspersed with iron phosphate phases on the surface of the sample. A phase containing Ce, Nd, O, and P was detected at the meniscus region of the Monofrax K-3 samples corroded in air. As this appears to be the same phase that was detected in the alumina air 4 h sample, an air environment appears to encourage the formation of this phase. The distribution of Si as shown in the EDS maps is influenced by the multiple sources of this component. Although SiO₂ is one component of Monofrax K-3. Si may have been present in the DPF5-336 from the fused quartz crucible used for corrosion testing.

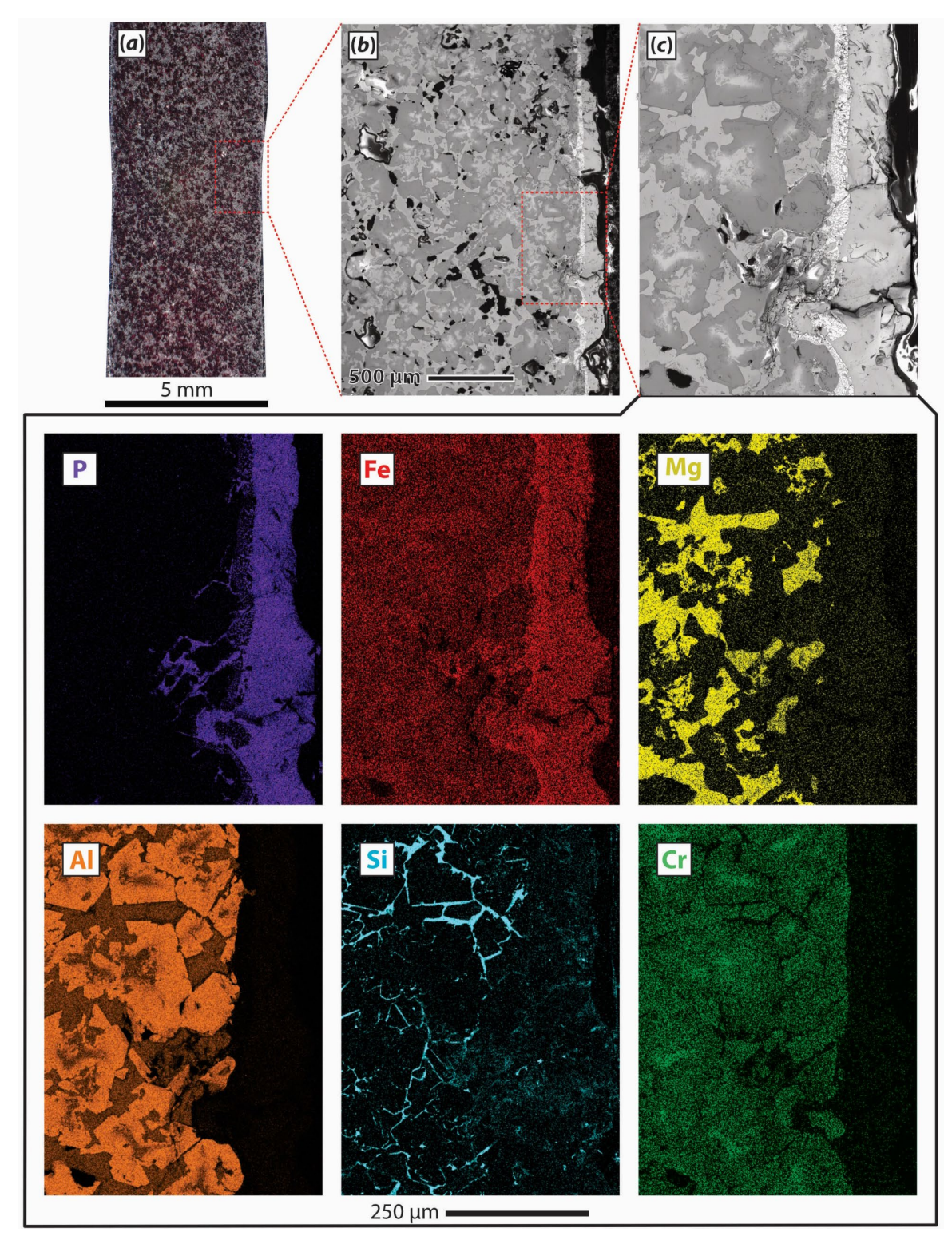


Figure 3-14. The K3-Air-1h sample is shown. The optical image in (a) shows corrosion of the bar in the meniscus region. (b) BSE image showing the bright corrosion layer at the bar edge. Dark regions are voids. The SEM/EDS maps in (c) indicate the penetration of DPF5-336 components beyond the corrosion layer.

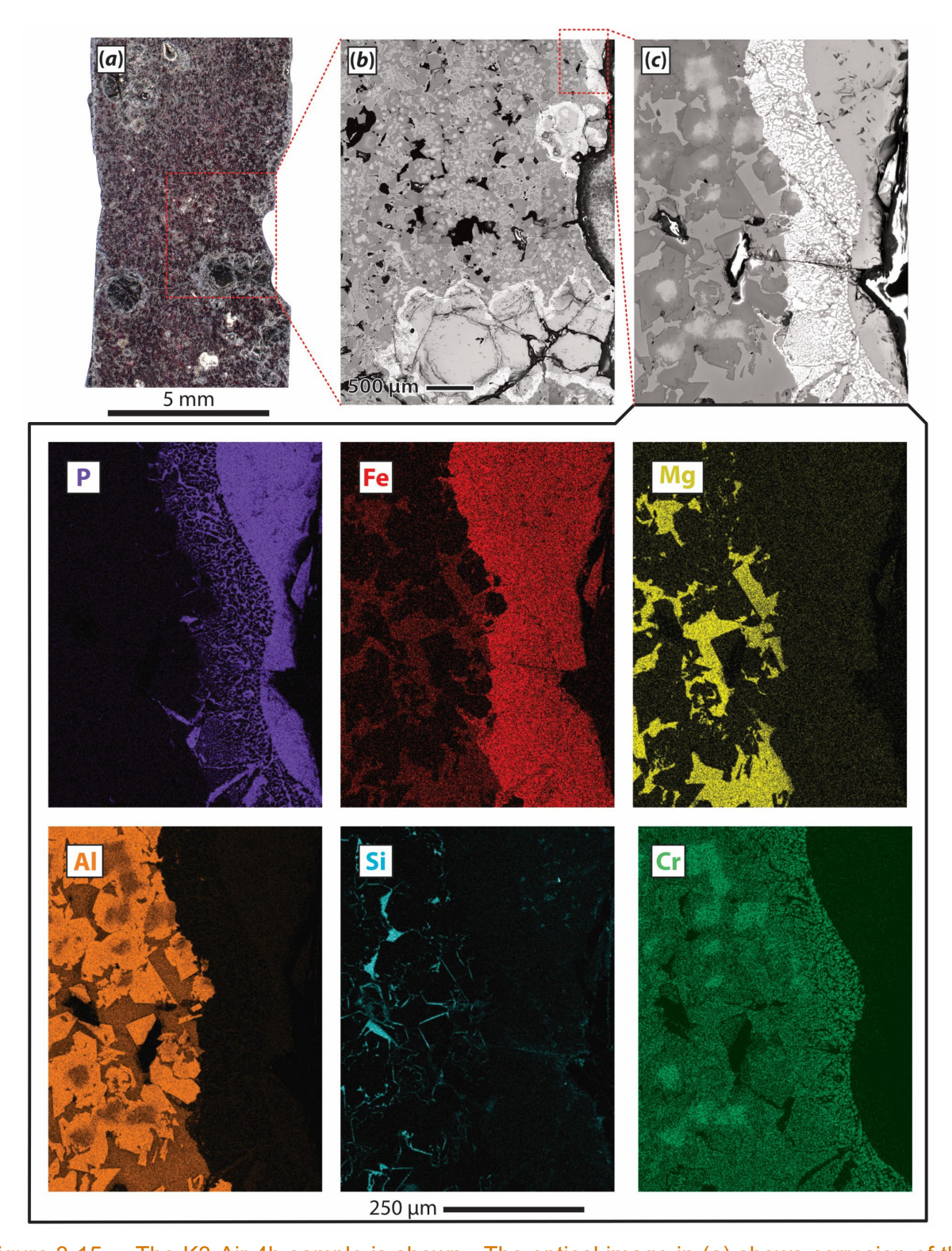


Figure 3-15. The K3-Air-4h sample is shown. The optical image in (a) shows corrosion of the bar in the meniscus region with visible penetration of DPF5-336. (b) BSE image showing the bright corrosion layer around light grey areas of DPF5-336. Dark regions are voids. The SEM/EDS maps in (c) indicate the penetration of DPF5-336 components beyond the corrosion layer.

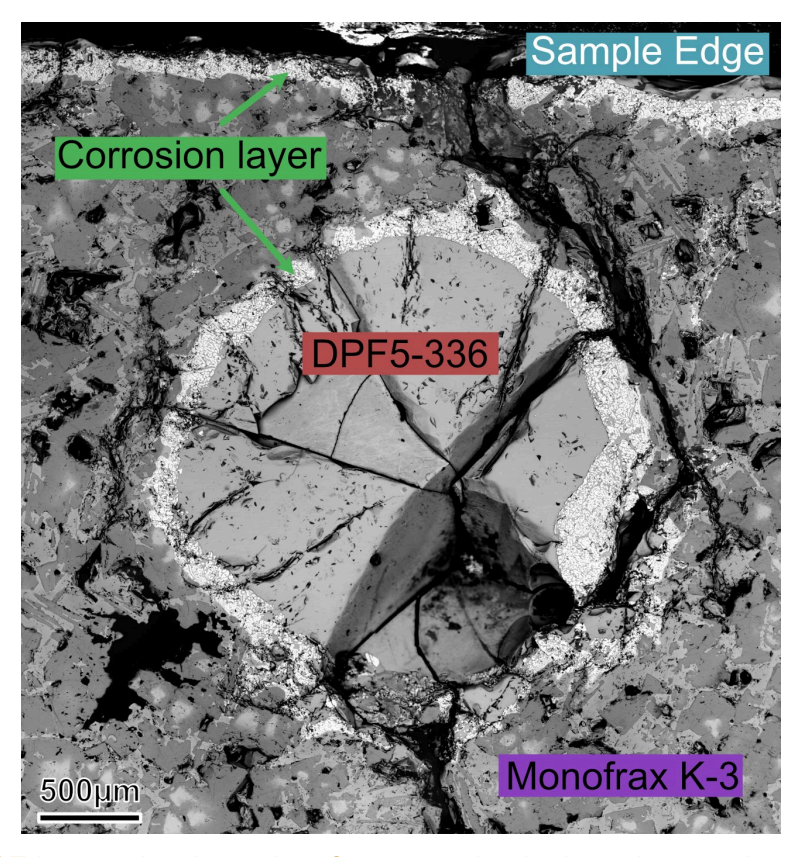


Figure 3-16. BSE image showing subsurface corrosion in the submerged region of the K3-Air-4h sample with regions of interest labelled.

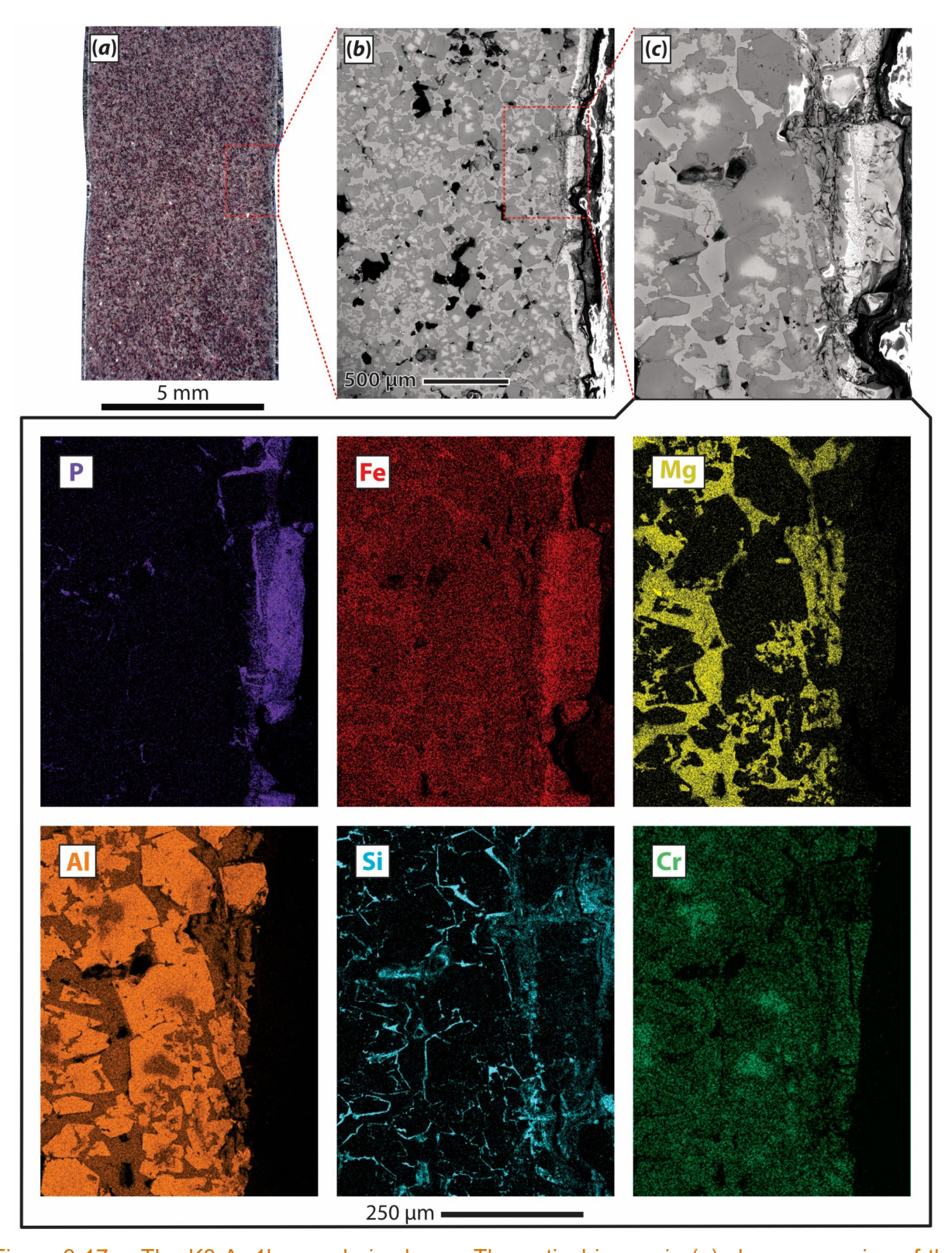


Figure 3-17. The K3-Ar-1h sample is shown. The optical image in (a) shows corrosion of the bar in the meniscus region. (b) BSE image showing the bright corrosion layer at the bar edge. Dark regions are voids. The SEM/EDS maps in (c) indicate the penetration of DPF5-336 components beyond the corrosion layer.

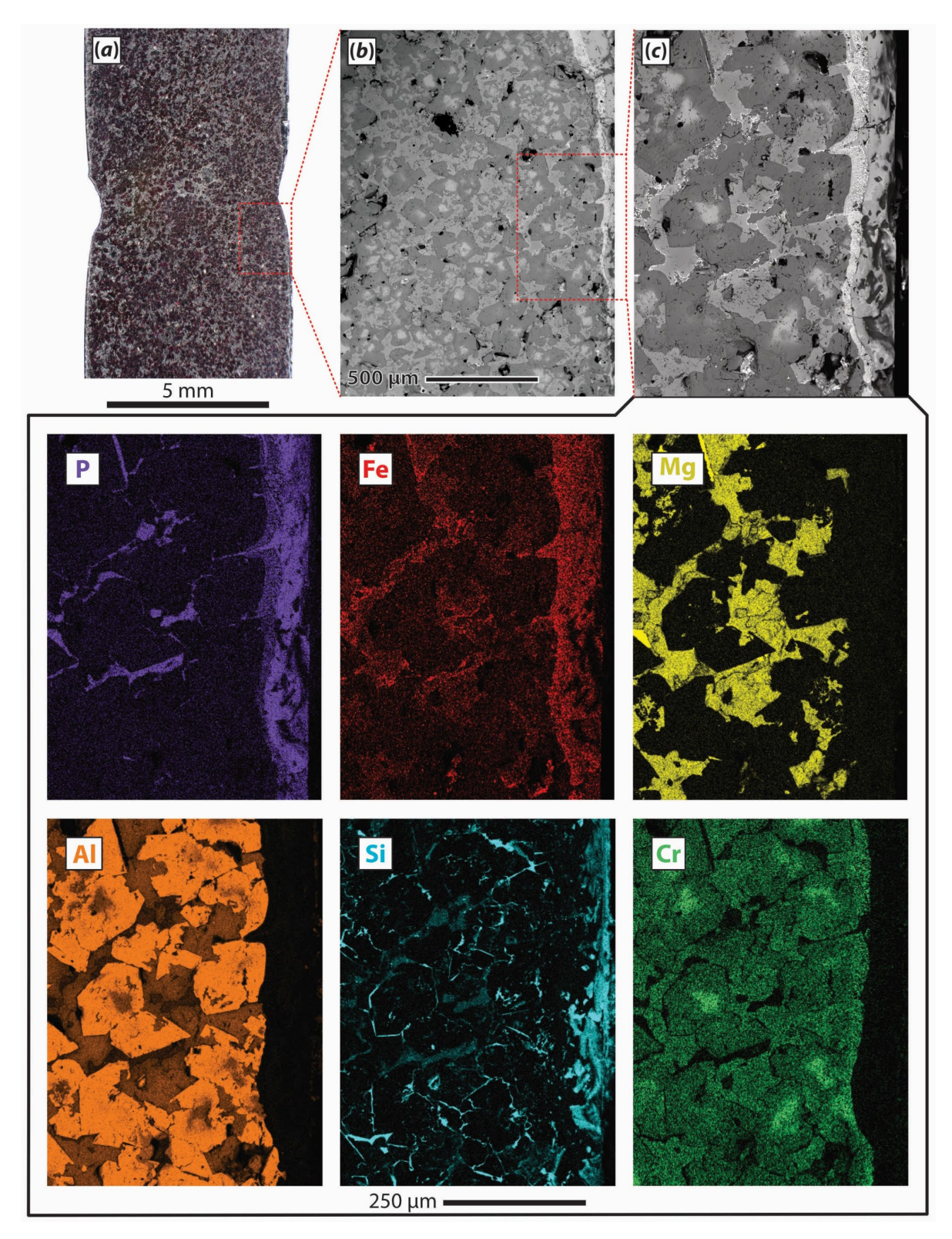


Figure 3-18. The K3-Ar-4h sample is shown. The optical image in (a) shows corrosion of the bar in the meniscus region. (b) BSE image of the meniscus region reveals a bright phase along the grain boundaries. The SEM/EDS maps in (c) confirmed the bright phase contained components from the DPF5-336 glass.

3.4 Stainless Steel 316L

Stainless steel 316L bars corroded extensively in both atmospheres; only the samples exposed for 1 h were sufficiently intact for subsequent analysis with data shown in Figure 3-19, Figure 3-20, and Figure 3-21. The sample corroded in air developed regions with a thick corrosion layer, as shown in Figure 3-19. The SEM/EDS maps in Figure 3-19b and Figure 3-20 reveal penetration of DPF5-336 components by intergranular corrosion. Mo and Ni migrated from the bulk of the bar to the metal adjacent to the corrosion layer. Formation of the Cr-rich corrosion layer depleted the adjacent metal of Cr. The corrosion layer was a heterogeneous mixture of the chromium oxide phase and a phase rich in Fe and P, with pockets of unoxidized metal within the layer consisting of Fe, P, Ni, and Mo. As shown in Figure 3-19, the thickness of the total affected region near the surface of the bar in contact with the molten DPF5-336 reached ≈ 1 mm in some areas. In comparison, the oxidized corrosion layer is thinner in the sample corroded in argon as shown in Figure 3-21, although the Cr depletion and Mo and Ni migration are still evident. Corrosion of the bar in argon was concentrated at the meniscus area of the molten DPF5-336, lacking the dispersed regions of extensive corrosion as seen in bar corroded in air.

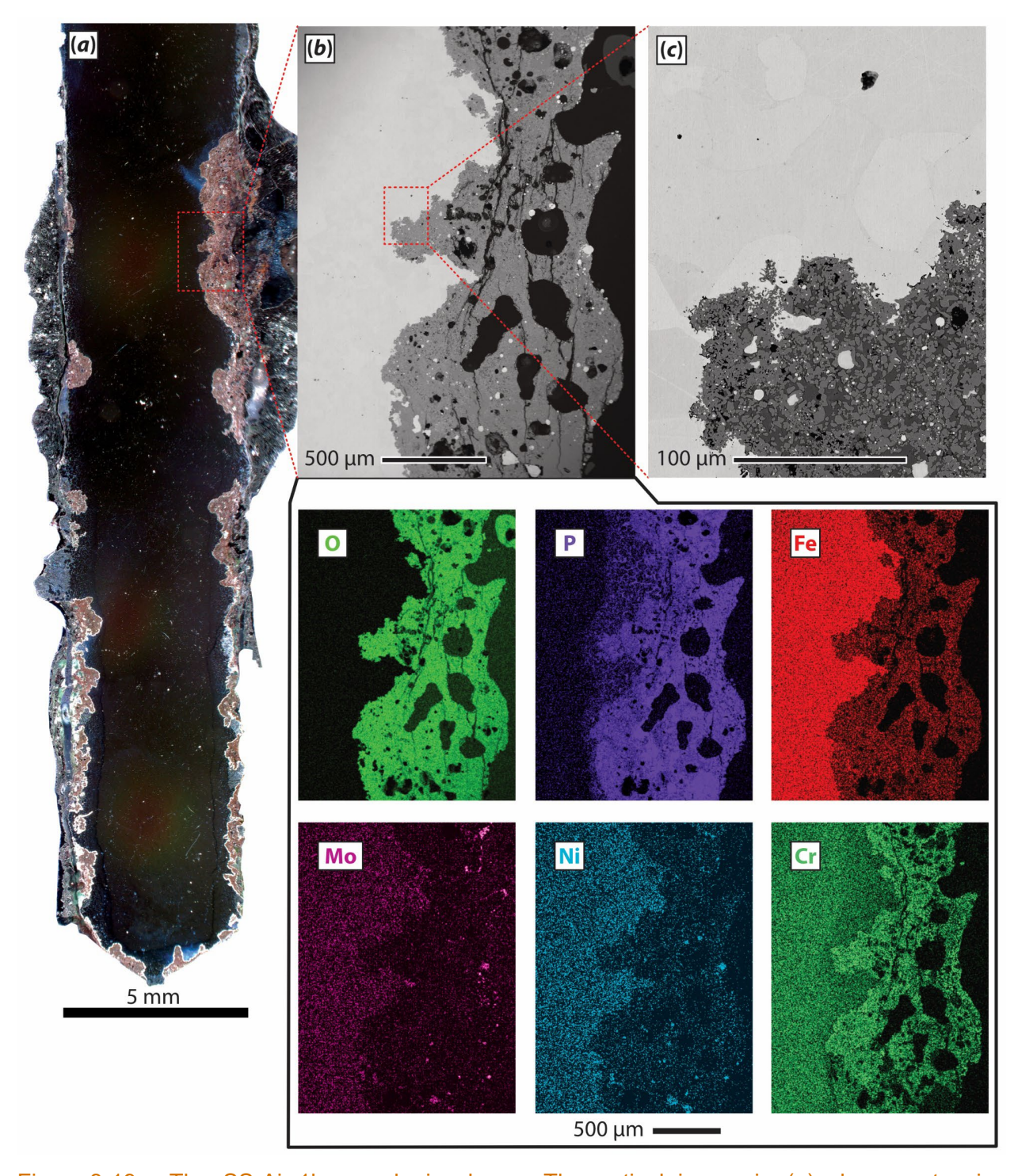


Figure 3-19. The SS-Air-1h sample is shown. The optical image in (a) shows extensive corrosion of all surfaces in contact with the molten glass. (b) SEM/EDS maps reveal the migration of components and formation of a corrosion layer. (c) shows the phase separation in the corrosion layer in greater detail.

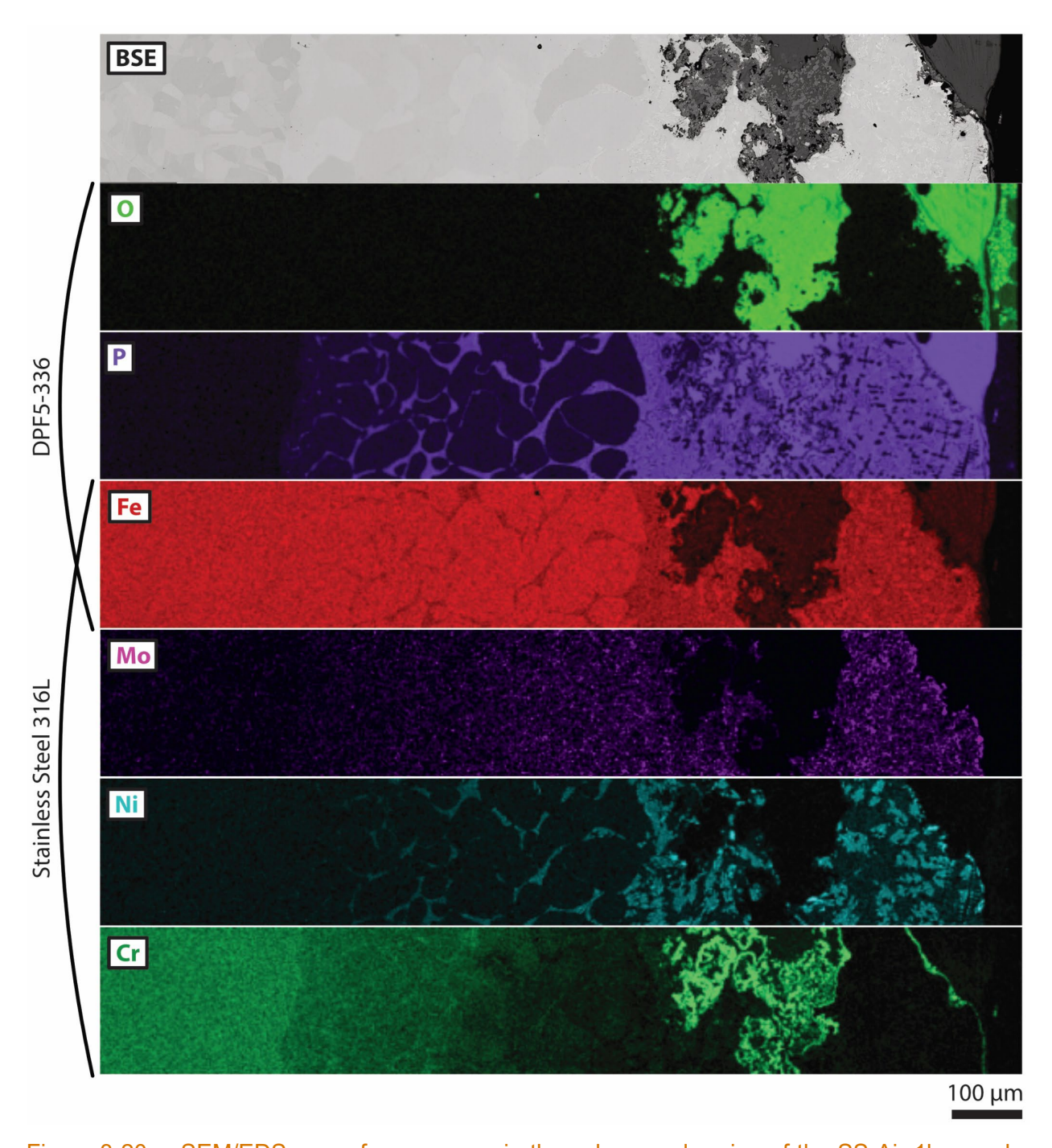


Figure 3-20. SEM/EDS maps from an area in the submerged region of the SS-Air-1h sample. The edge of the bar that was in contact with the molten glass is oriented to the right. Labels on the left indicate the source of each component.

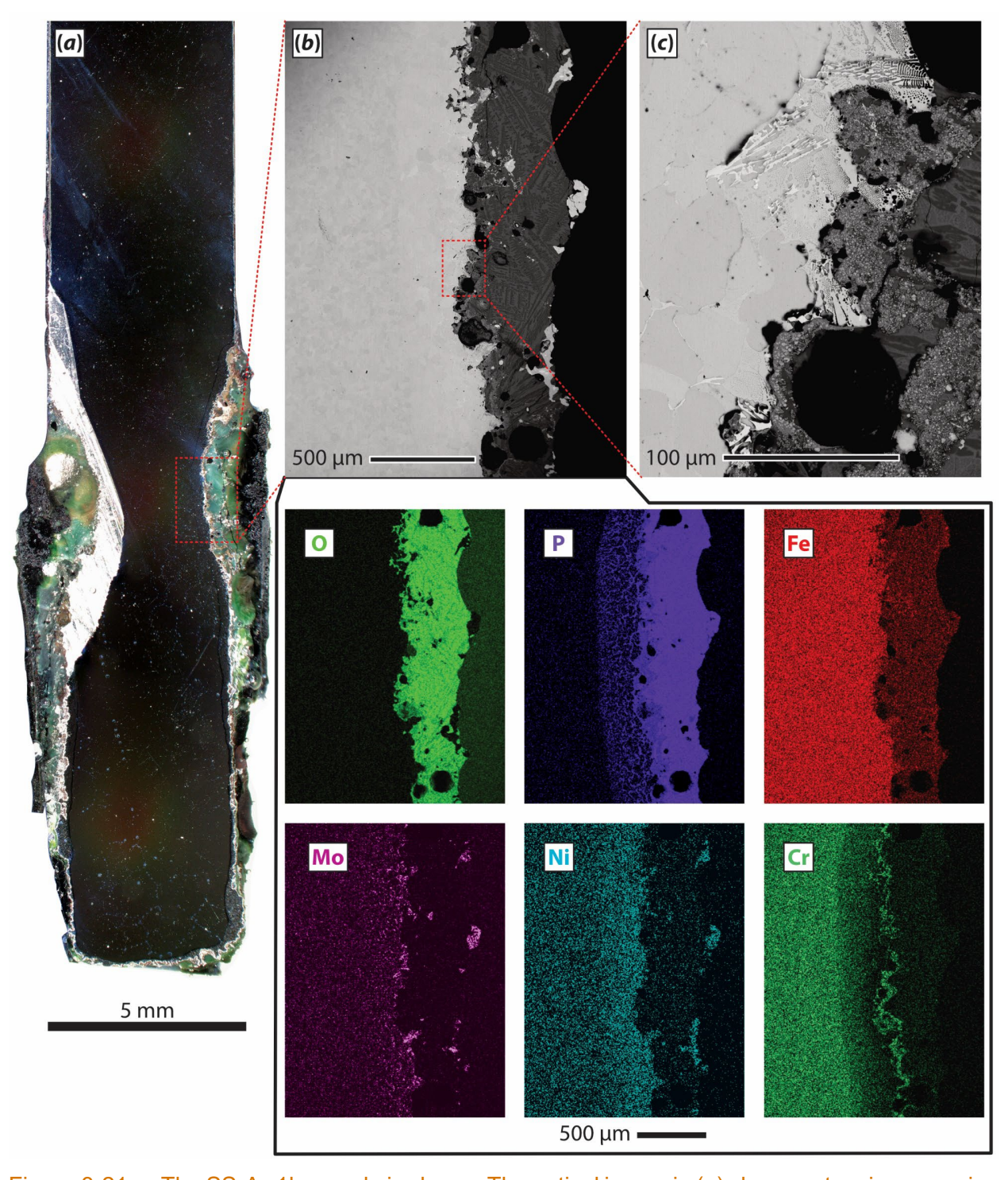


Figure 3-21. The SS-Ar-1h sample is shown. The optical image in (a) shows extensive corrosion of the bar in the meniscus region. (b) SEM/EDS maps reveal the migration of components and formation of a corrosion layer. (c) SEM of the phase separation in the corrosion layer shown in greater detail.

3.5 Inconel 693

The Inconel 693 bars corroded extensively in both atmospheres with data shown in Figure 3-22, Figure 3-23, and Figure 3-24. The specimen run in air corroded extensively and separated into two sections during analysis, while the bar in argon lost 28.34 mm² of material from the neck region. The greatest depth of penetration into the bulk of the bar was ≈ 100 µm in either atmosphere. Regions of penetration (as determined by phosphorus detection) were enriched in Ni and depleted of Cr and Al, as shown in the EDS maps in Figure 3-22, Figure 3-23, and Figure 3-24. Corrosion products are heterogeneously dispersed and consist of fragmented sections of metal with a composition like the penetrated region of the bar edge, Cr-rich and Al-rich oxide(s), and iron phosphate phases resulting from crystallization of DPF5-336, possibly with incorporation of Inconel components.

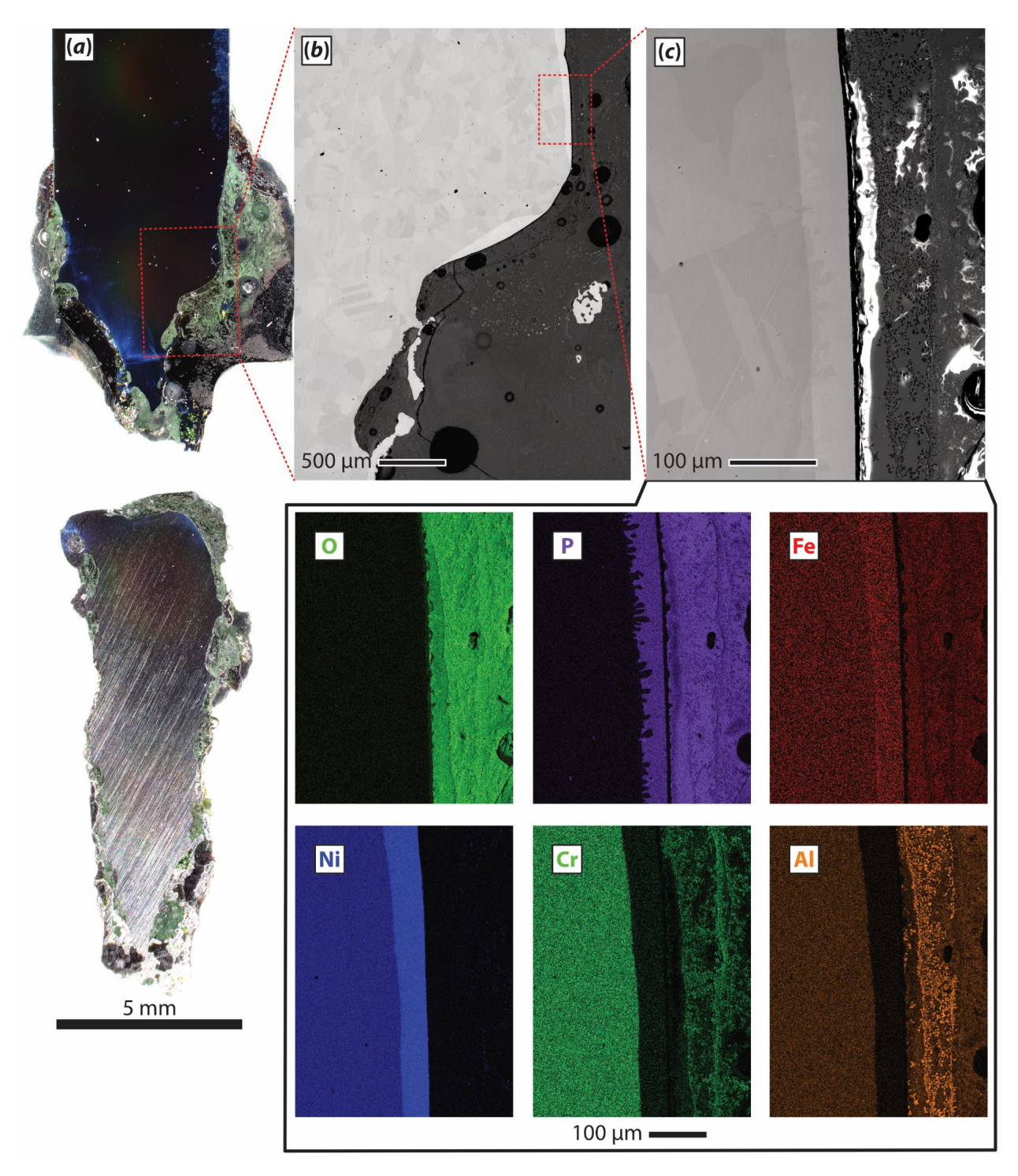


Figure 3-22. The Inconel-Air-1h sample is shown. The sample separated into two pieces during preparation for analysis. The optical image in (a) shows extensive corrosion of all surfaces in contact with the molten glass. The (b) BSE-SEM micrograph of the bar edge and (c) SEM/EDS maps reveal the migration of components and formation of a corrosion layer.

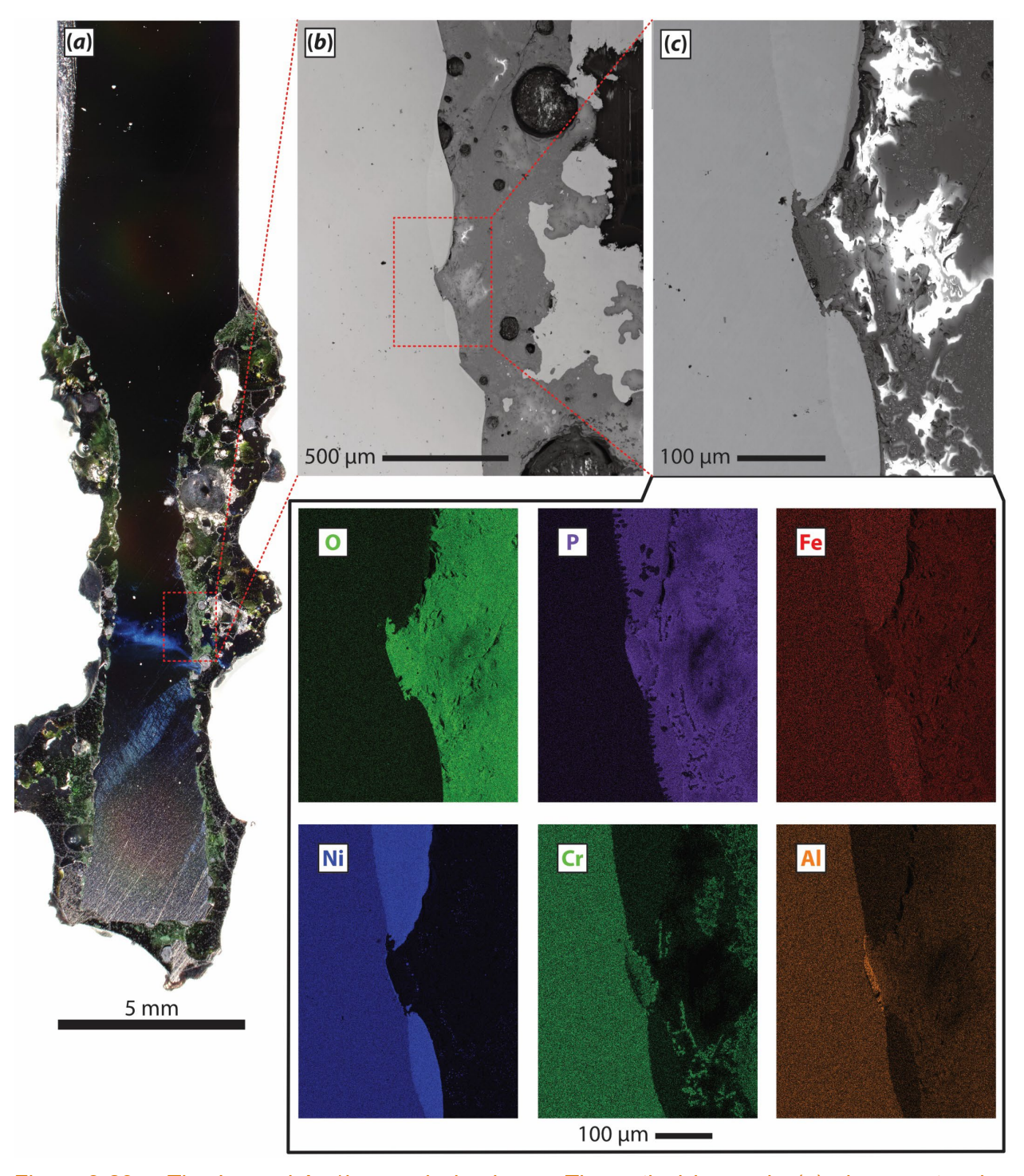


Figure 3-23. The Inconel-Ar-1h sample is shown. The optical image in (a) shows extensive corrosion of all surfaces in contact with the molten glass. The (b) BSE-SEM micrograph of the bar edge and (c) SEM/EDS maps reveal the migration of components and formation of a corrosion layer.

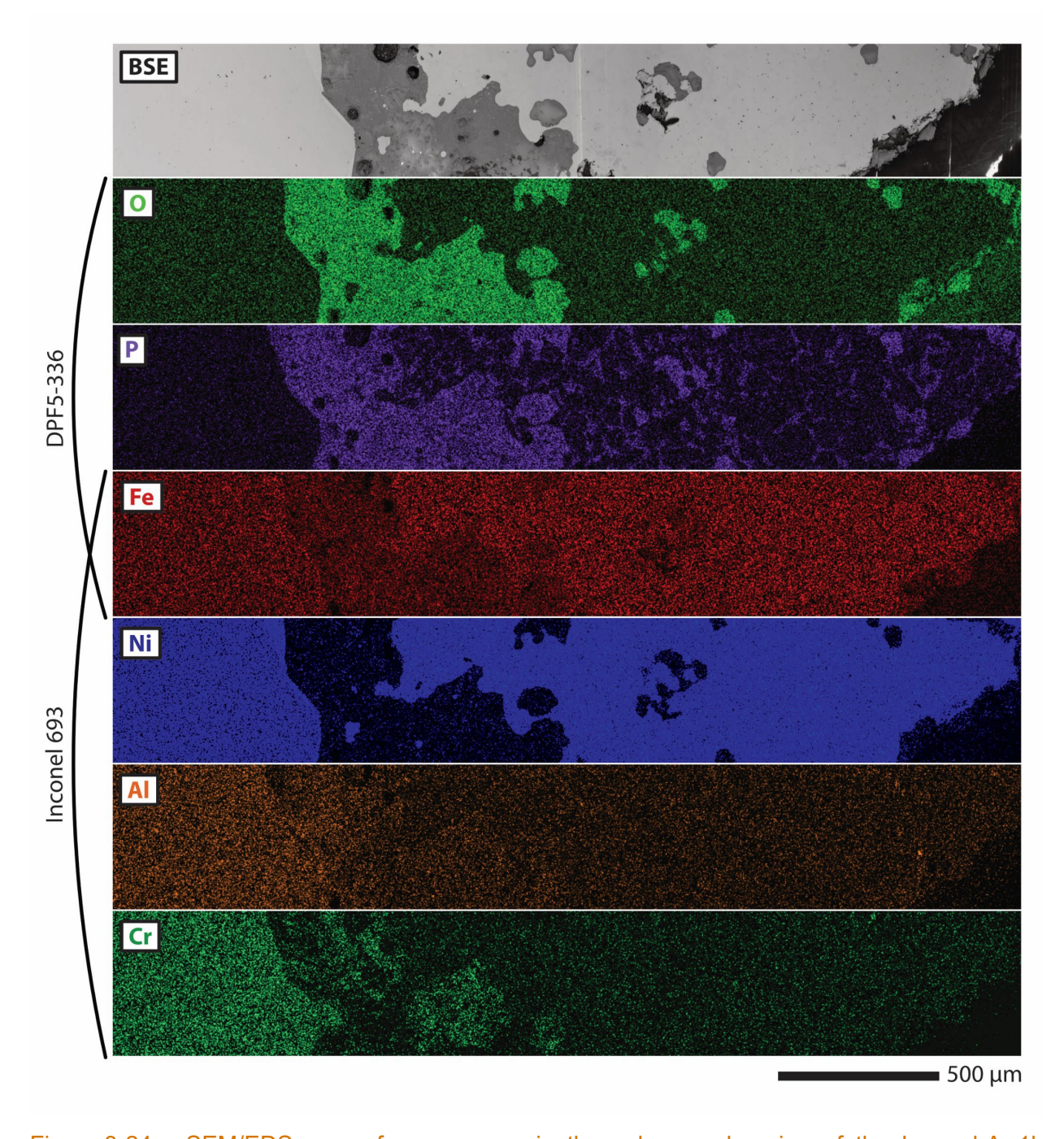


Figure 3-24. SEM/EDS maps from an area in the submerged region of the Inconel-Ar-1h sample. The edge of the bar that was in contact with the molten glass is oriented to the right. Labels on the left indicate the source of each component.

4.0 Waste Form Synthesis

At the time the projected started, the waste form design task was primarily focused on finding glass-forming regions within the iron phosphate system with suitable chemical durabilities. While regions had previously been identified (Day et al. 1998; Brow et al. 2020; Riley et al. 2020; Chong and Riley 2024; Marcial et al. 2024), results were mostly based on quenched glasses. As phosphate separation and crystallization are often observed upon cooling, and especially during CCC treatment, regions with high thermal stabilities were identified first with the SSM using slow-cooling heat treatments. Glass forming compositions were selected for additional study and characterization.

For the preparation of iron-phosphate waste forms, a simple salt mixture was dechlorinated with H_3PO_4 using a heating profile modified from Murray et al. (2024) such that isothermal holds at 100°C and 200°C were 45 min and additional holds were 30 min to obtain the dechlorinated product (DP). Samples were prepared with a dechlorination heating profile that terminated at either 400°C or 600°C (DP-400 and DP-600, respectively). Glass forming materials H_3PO_4 (Fisher Chemical 85% w/w), Fe_2O_3 (Sigma Aldrich > 99%), Li_2CO_3 (Tokyo Chemical Industry >98.09%), Na_2CO_3 (VWR, 99.5%), and K_2CO_3 (Thermo Scientific 99%) were added to the dechlorinated product and the mixture was vitrified by heating at 10°C·min⁻¹ to 1050°C with an isothermal hold at 1050°C for 1 h, as shown in Figure 4-1. Both dechlorination and vitrification were performed in silica crucibles (AdValue, high form, FQ-1050). SSM-DP and Dechlorinated Simple Salt Mixture Phosphate+ Fe_2O_3 (SSM-DPF) target compositions investigated from the study are listed in Table 4-1. Where the dechlorination processing parameters are relevant, samples that were prepared with a dechlorination heating profile that terminated at 400°C or 600°C are discussed as SSM-DPF-400 and SSM-DPF-600, respectively.

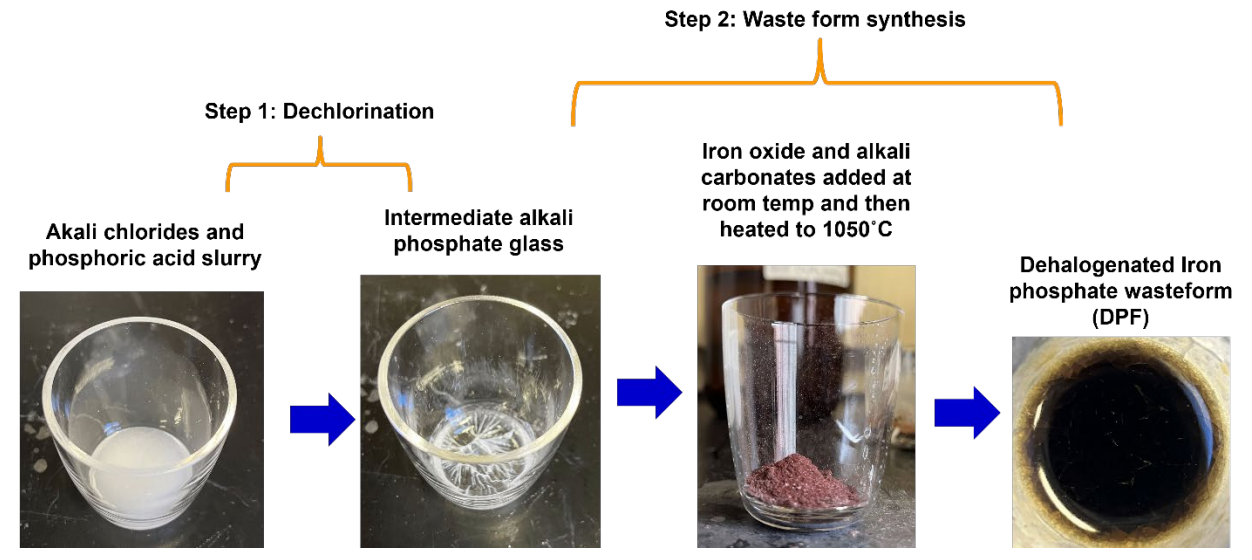


Figure 4-1. The formation of DPF samples from a simple salt waste simulant is shown in the schematic as a two-step process involving separate dechlorination and vitrification steps.

Table 4-1. SSM-DP and SSM-DPF target compositions prepared in this study are shown. Calculations assumed all cations in the initial batch form oxides (e.g. all LiCl and Li₂CO₃ in the batch form Li₂O) and only trivalent iron is present. A₂O denotes total alkali oxide content.

Sample ID	Target Composition (mol%)							Theoretical Ratios (molar)	
	Li ₂ O	K ₂ O	Na ₂ O	Total A ₂ O	Fe ₂ O ₃	P_2O_5	Fe/P	O/P	
SSM-DP	0.2402	0.1666	0.0932	0.5000	0.0000	0.5000	0.0000	3.0000	
SSM-DPF2	0.2570	0.1783	0.0997	0.5350	0.0536	0.4114	0.1303	3.3457	
SSM-DPF3	0.2560	0.1776	0.0994	0.5330	0.0801	0.3870	0.2069	3.4990	
SSM-DPF4	0.2550	0.1769	0.0990	0.5309	0.1063	0.3628	0.2932	3.6715	
SSM-DPF5	0.2540	0.1762	0.0986	0.5288	0.1324	0.3387	0.3909	3.8669	
SSM-DPF6	0.2530	0.1756	0.0982	0.5268	0.1583	0.3149	0.5025	4.0902	
SSM-DPF7	0.2401	0.1666	0.0932	0.4998	0.2173	0.2829	0.7680	4.5351	
SSM-DPF8	0.2542	0.1763	0.0986	0.5292	0.0555	0.4153	0.1337	3.3376	
SSM-DPF9	0.2445	0.1697	0.0949	0.5091	0.1647	0.3262	0.5050	4.0378	
SSM-DPF10	0.2494	0.1730	0.0968	0.5192	0.1102	0.3706	0.2975	3.6468	
SSM-DPF11	0.1506	0.1045	0.0584	0.3134	0.4187	0.2678	1.5635	5.4304	
SSM-DPF12	0.2015	0.1398	0.0782	0.4194	0.1409	0.4396	0.3206	3.4579	
SSM-DPF13	0.1619	0.1123	0.0628	0.3371	0.2252	0.4377	0.5146	3.6570	
SSM-DPF14	0.1735	0.1204	0.0674	0.3613	0.2774	0.3613	0.7680	4.1519	

The compositional space was restricted to compositions that would be suitable for the theoretical stoichiometric reaction to form a fully dechlorinated product (i.e. P/Cl ≥ 1 in the starting batch for dechlorination). As phosphate addition complicates processing, only two compositions that required phosphate addition were examined; other compositions required only the addition of iron oxides and carbonates as shown in Figure 4-2. The exact type and quantity of material additions required to reach the desired waste form composition were predetermined by the P/Cl ratio selected for the SSM-DP.

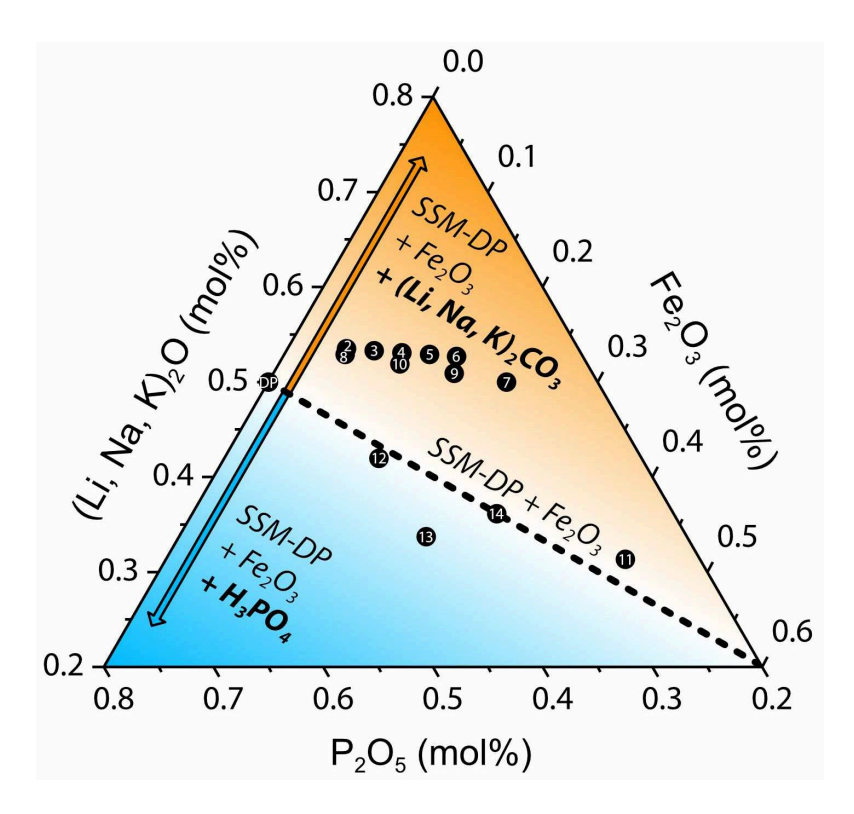


Figure 4-2. Ternary diagram of SSM-DPF target compositions with regions labeled according to the required material additions to the SSM-DP before vitrification. The dashed line indicates target compositions that would require only Fe₂O₃ additions to the SSM-DP. SSM-DPF14 lies on the dashed line. Compositions in the region above the dashed line (colored orange) require the addition of both Fe₂O₃ and alkali carbonates. Compositions in the region below the dashed line (colored blue) require the addition of both Fe₂O₃ and a phosphate precursor (H₃PO₄ was used in this work).

The ternary diagram in Figure 4-3 shows samples and their corresponding composition. Only SSM-DPF11 did not melt completely during the vitrification step, containing large metallic lumps in the center of the sample due to the large amount of Fe₂O₃ added for that composition. Compositions SSM-DPF2, SSM-DPF3, SSM-DPF8, and SSM-DPF10 appear glassy and all other SSM-DPF compositions presented here appear partially or wholly crystalline. Samples were ground in a tungsten carbide milling chamber and XRD analysis was performed with a Bruker D8 Advance (BrukerAXS Inc., Madison, WI) equipped with a Cu K α target (λ = 1.5406 Å) and a LynxEyeTM position-sensitive detector at 40 kV and 40 mA. Powders of each sample were scanned from 5–70° (2 θ), with a step size of 0.015° (2 θ), and a dwell of 2 s per step. The XRD scans of SSM-DPFs confirmed the amorphous structure of SSM-DPF2, SSM-DPF3, SSM-DPF8, and SSM-DPF10 as shown in Figure 4-5. XRD scans of crystallized samples are shown in Figure A-1 (Appendix A).

Variations in processing conditions were investigated for the SSM-DPF10 composition. SSM-DPF10-400 and SSM-DPF10-600 (not shown) had an identical visual appearance. An SSM-DPF10-400 sample prepared under an argon atmosphere yielded a metallic surface color as shown in Figure 4-4. Cross sections of the SSM-DPF10 prepared in argon appeared brown in color, akin to the sample prepared in air. Therefore, the metallic surface appearance of the SSM-DPF10 prepared in argon suggests that iron was reduced at the sample surface.

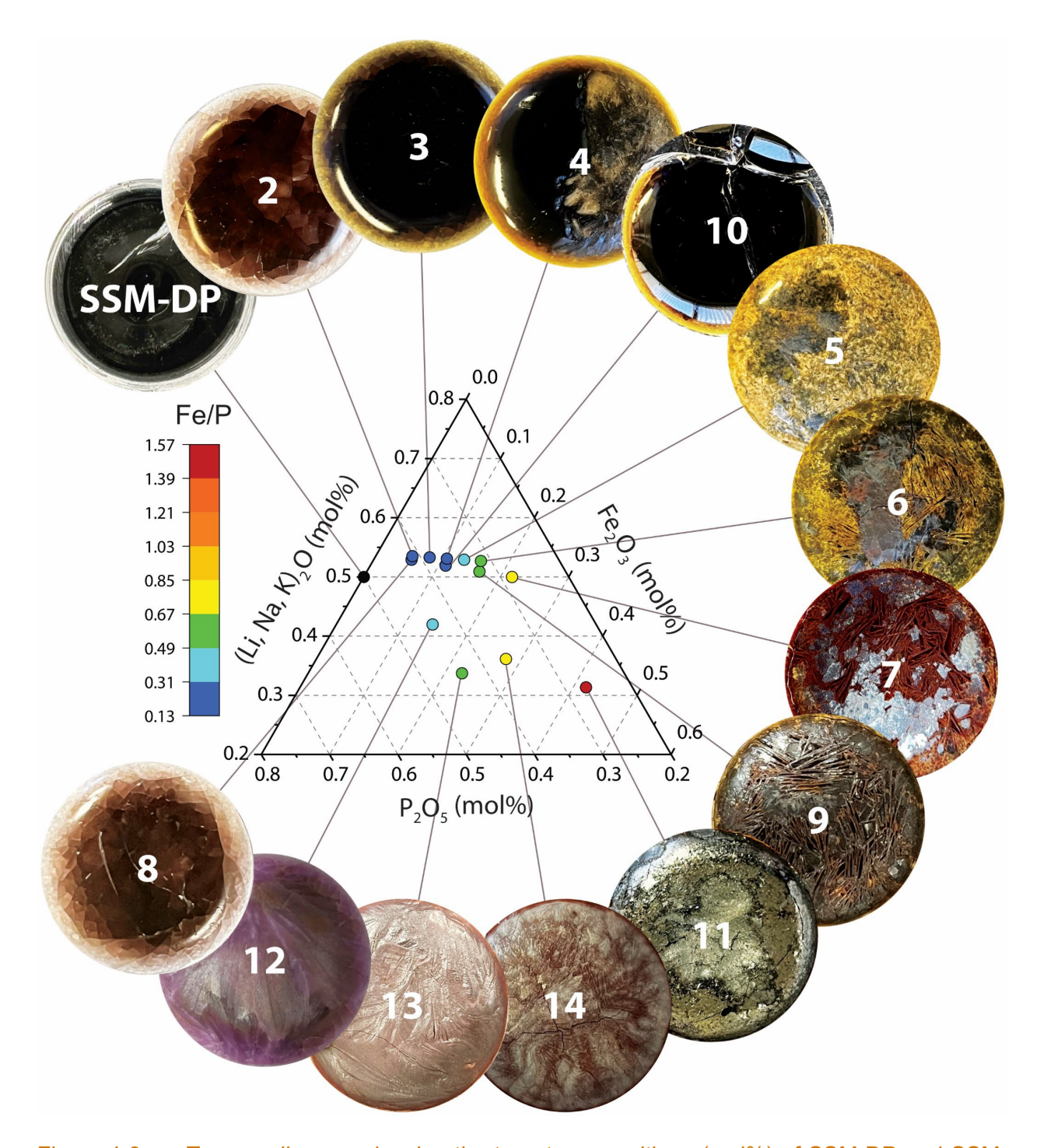


Figure 4-3. Ternary diagram showing the target compositions (mol%) of SSM-DP and SSM-DPFs prepared in this work. Images of the waste forms and their associated sample ID are shown in callouts. Composition markers on the ternary diagram are colored according to their theoretical Fe/P ratio. SSM-DPF7 and SSM-DPF11— SSM-DPF14 were made with an SSM-DP dechlorinated at 600°C and all others were made using an SSM-DP dechlorinated at 400°C.

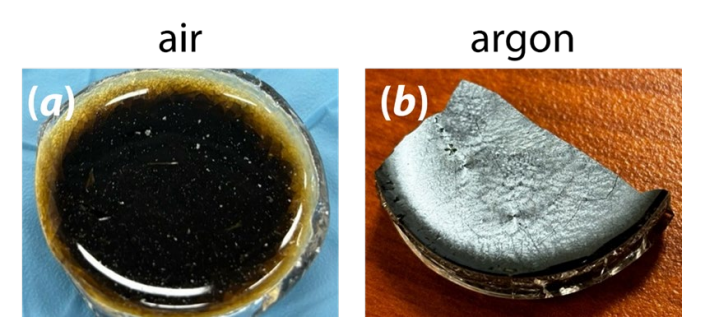


Figure 4-4. SS-DPF10-400 vitrified in (a) air and (b) argon atmospheres. The air sample surface is dark, while the argon sample has a shiny, grey surface with a metallic appearance. It is hypothesized that the difference is caused by a thin crystallized surface layer such as Fe₂O₃ for the sample prepared in argon based on similar observations from a previous study (Riley et al. 2020).

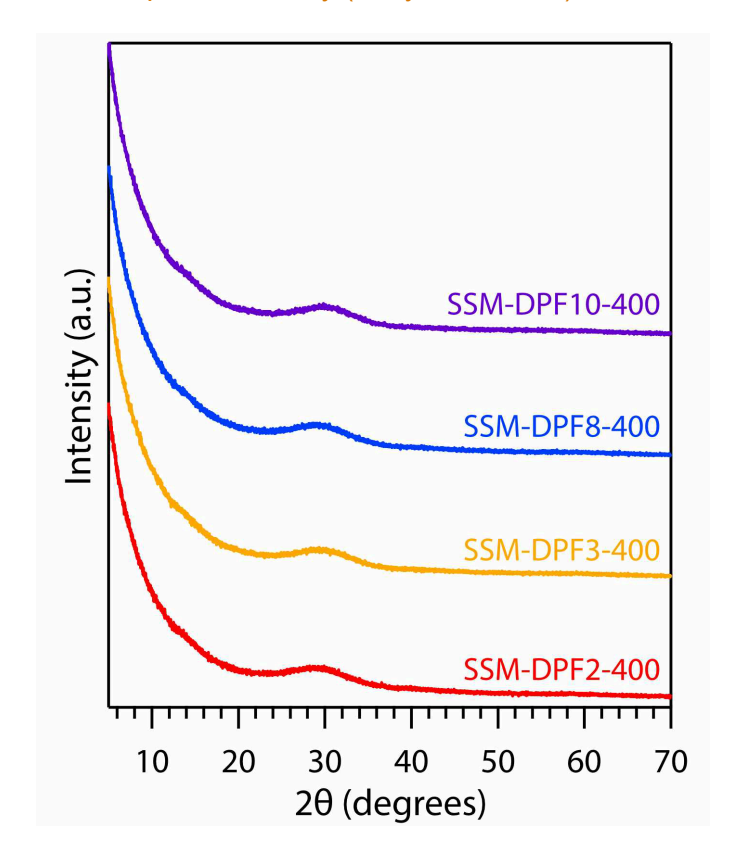


Figure 4-5. XRD scans of SSM-DPFs show four amorphous samples as labelled.

Cross-sections of SSM-DPF8—SSM-DPF10 were prepared with a 10 nm gold coating for scanning electron microscopy with energy dispersive X-ray spectroscopy (SEM/EDS) to examine phase separation in the samples. EDS analysis was performed using a Thermo Scientific Scios 2 focused ion beam SEM with an accelerating voltage of 20.00 kV and a beam current of 3.2 nA. The backscattered electron (BSE) SEM micrographs in Figure 4-6 show bright regions in the BSE image in that correspond to areas with a higher average atomic number (e.g., high-Fe). According to the EDS maps, these areas also contain P and overlap with high K and Na concentrations, indicating alkali iron phosphate phases. Fe, Na, and K are homogenously distributed in the phosphate glass phase in Figure 4-6b and Figure 4-6c. In Figure 4-6b, dark spots in the BSE

image correspond to Fe-deficient regions. A comparison with the Si EDS map reveals that these regions are Si-rich droplets that exclude the other components. Examining the Si EDS maps in Figure 4-6a-c reveals the presence of SiO₂-rich phase-separated droplets in all three samples.

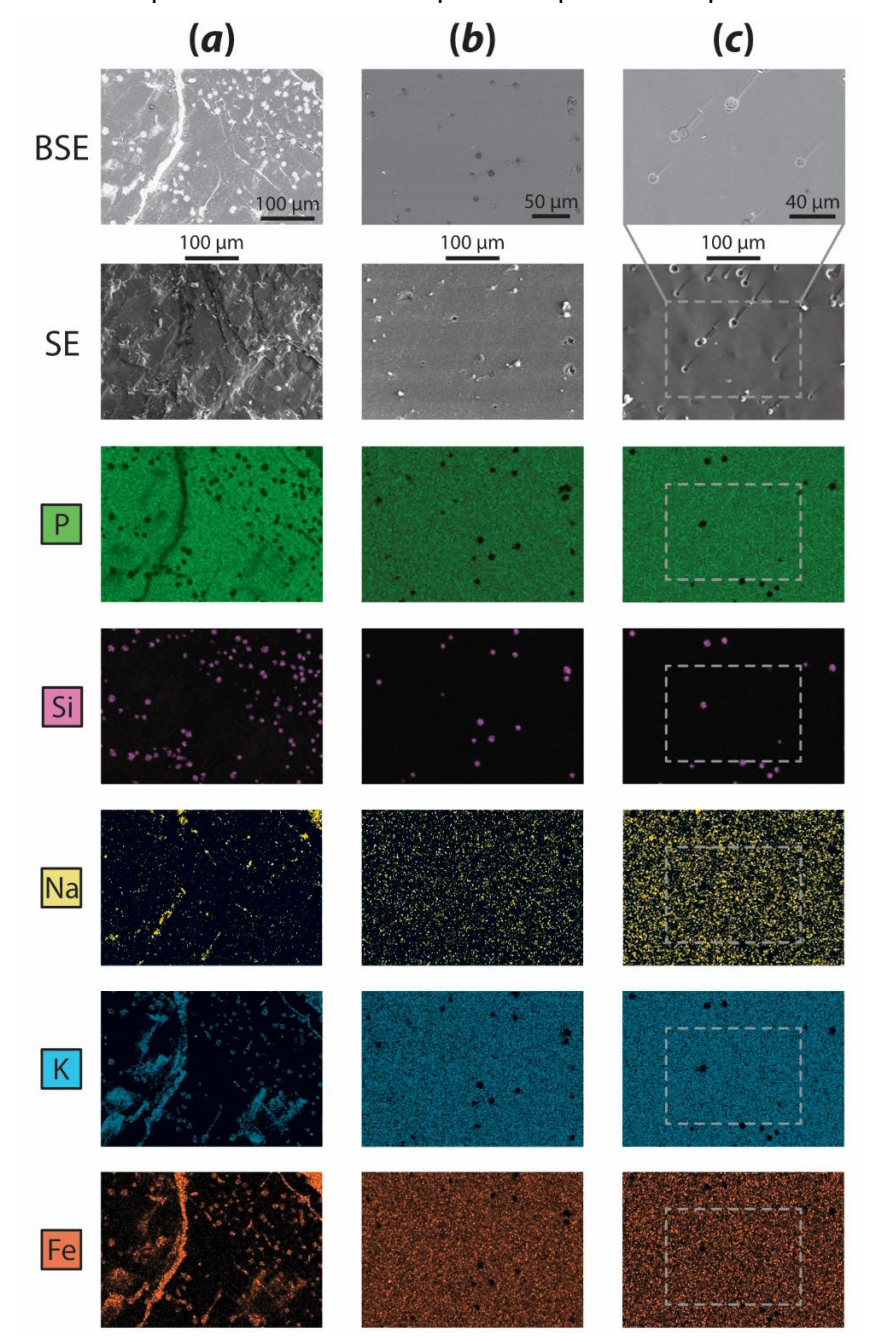


Figure 4-6. SEM images and EDS maps of the cross-sections of (a) SSM-DPF9-400 (b) SSMDPF-10-400 and (c) SSM-DPF8-400. The dashed boxes in (c) show the corresponding BSE image boundary. All samples show phase-separated Si droplets.

The secondary electron (SE) image in Figure 4-6c shows Si droplets physically separated from the rest of the sample during preparation for SEM analysis. The Si content is from degradation of the silica crucible during dechlorination, as discussed in Section 2.0. It is suspected that additional

Si degradation occurred during vitrification. Amorphous phase separation of Si and P phases is expected, as high Fe and alkali content promote SiO₂-P₂O₅ immiscibility.

Similar observations of SiO₂-rich droplets within a phosphate matrix were made in a previous study by Evarts et al. (2025a) where borosilicate glasses were added to DP products to improve chemical durability. In the study by Evarts et al. (2025a), authors induced phase separation of silica droplets for improved fission product separation/sequestration by the addition 2.5–30 mass% of a borosilicate frit to DPF compositions. Therefore, the silica droplets have important implications for the DPFs and the inclusion of the crucible material into the SSM-DPs and SSM-DPs reflects an essential processing consideration for both steps in the dechlorination treatment method. The clear detrimental issue is that incorporation of SiO₂ into the melt means that the containment is dissolving, thereby thinning the walls of the melt containment. If the containment is compromised, it will infiltrate the furnace and cause damage. If this were to happen in a large-scale operation, especially one where radioactive material is involved, that would be a major issue for containment among other issues.

As one of the glass forming compositions in this study, SSM-DPF10 was selected for further analysis. An SSM-DPF10-400 sample was examined with simultaneous differential scanning calorimetry (DSC) and thermogravimetric analysis (TGA) (Netzsch 449-F3 Jupiter simultaneous thermal analyzer). A section of the SSM-DPF was placed in an alumina-lined Pt-Rh pan with a Pt lid. The sample was heated to 800°C at a rate of 20°C min⁻¹ under ultra-high purity (99.999%) argon flowing at 70 mL min-1. Figure 4-7 shows the DSC/TGA results from SSM-DPF10-400 with the characteristic temperatures labelled. An endothermic peak after the glass transition temperature (T_q) indicates relaxation of the sample because of the slow cooling rate after vitrification. The T_g was determined to be 381.1°C, which matches well with Na₂O-Fe₂O₃-P₂O₅ glasses studied by Parsons and Rudd (2008). Compositions with similar alkali oxide content and Fe/P ratio to SSM-DPF10 had $T_{\rm g}$ values between 378-409°C (Parsons and Rudd 2008), indicating that the exact alkali mixture in SSM has little impact on T_q of this composition. These results are in accordance with work that has determined that iron phosphate glasses do not exhibit a mixedalkali effect for glass transition properties (Shelby 1975; Fang et al. 2003). The TGA trace reveals a 0.42% mass loss after melting, which may be attributed to the volatilization of residual HCl, Cl₂, or H₂O from the dechlorination processing step.

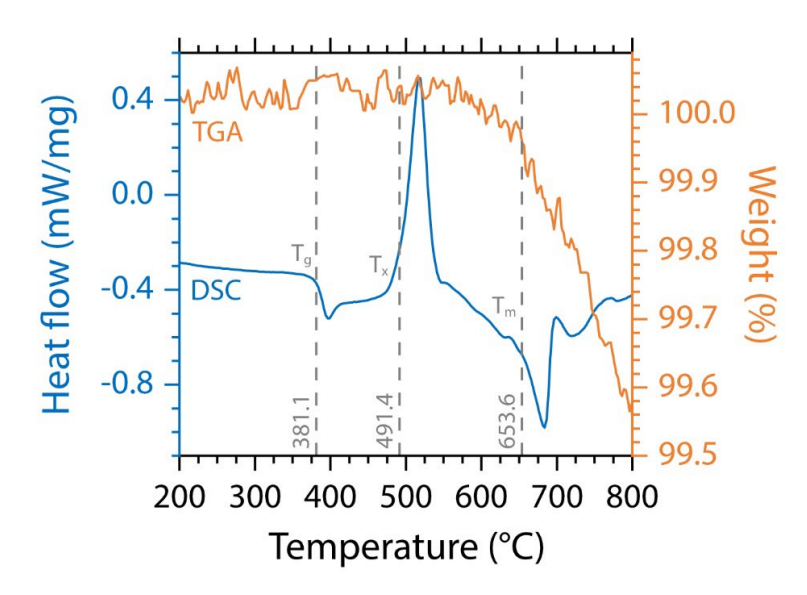


Figure 4-7. Simultaneous DSC/TGA of SSM-DPF10-400. Dashed lines mark the temperatures of the glass transition temperature (T_g), the onset of crystallization (T_x), and the melting temperature (T_m).

Additional characterization of the structure of the SSM-DPF10 composition was conducted with Mössbauer to study Fe²⁺/Fe³⁺ ratios, which are indicative of the properties of the waste form. The ⁵⁷Fe Mössbauer spectra were collected in transmission configuration at room temperature using a conventional constant acceleration spectrometer with a 50 mCi ⁵⁷Co y-ray source embedded in a rhodium matrix. The velocity scale of the spectrometer was calibrated using a spectrum from an α-Fe foil. Recoil software was used for optimizing sample thickness and fitting the Mössbauer spectrum for each glass. Approximately 30-50 mg of glass powder (< 75 um) was loaded into a lead sample holder with an aperture of 1 cm (diameter). The absorption spectra were fitted by Lorentzian multiplet analyses and the distribution of hyperfine parameters was estimated by using two symmetric quadruple doublets for each Fe-polyhedral site. The isomer shift (IS), quadrupole splitting (QS), total spectral area (A), and the full width at half maximum (FWHM) of each peak were allowed to vary until a best-fit solution was achieved. The weighted average values of the hyperfine parameters were reported. The Mössbauer results of SSM-DPF10-400 in Figure 4-8 indicate that the sample was dominated by Fe3+, indicating theoretical values based on the assumption of trivalent iron should be in good agreement with the measured composition of the sample.

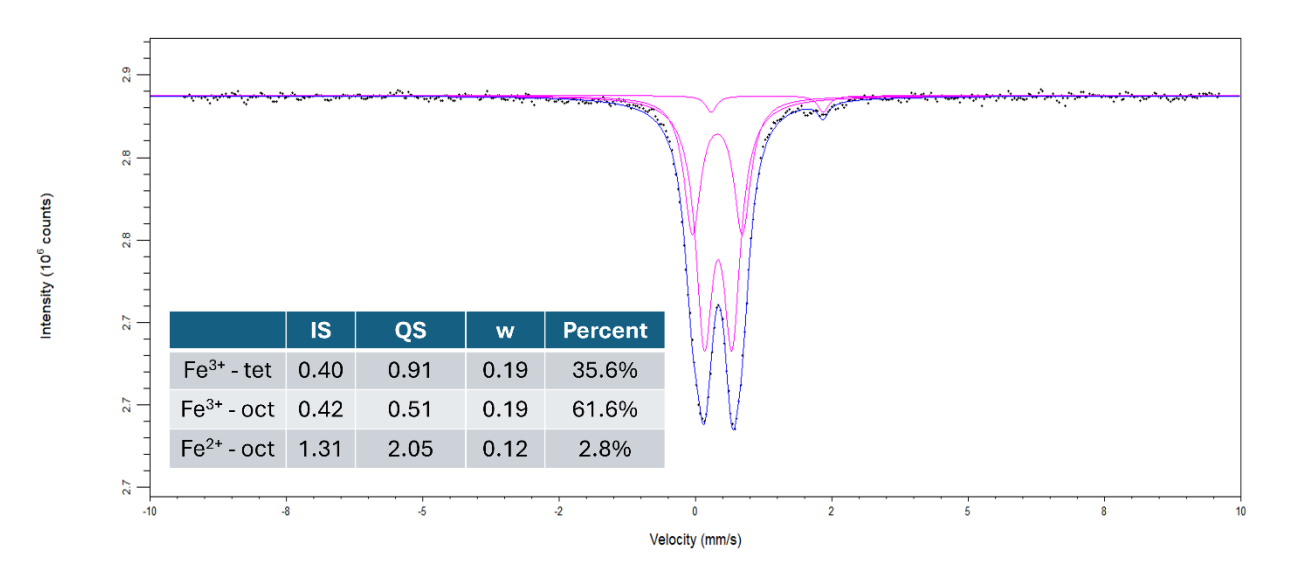


Figure 4-8. Mössbauer spectrum of SS-DPF10-400 with the results in the inset table.

High-performance liquid chromatography (HPLC, Dionex ion chromatography system) experiments were done to study the chain length distribution of phosphate anions in the glasses. Glass powders (75–150 μ m, 200 mg) were dissolved in an aqueous solution (50 mL) with 0.22 M NaCl + 5 mM Na4EDTA (ethylenediaminetetraacetic acid) and a pH of 10. EDTA was added as a chelating agent was added to slow the hydrolysis of phosphate chains in solution to facilitate analysis. SSM-DPF10 samples were prepared with variations in the DP dechlorination heating profile in order to investigate the impact of dechlorination processing parameters of the O/P ratio in the final waste form. The "continuous" heating profile type is described in Section 2.0, while "isothermal" indicates the heating profile used throughout this section. Parameters and the resulting O/P are listed in Table 4-2. The O/P ratio of the SSM-DPF10 samples did not change significantly regardless of environment or processing conditions during dechlorination. All samples were determined to have an O/P ratio close to the theoretical value given in Table 4-2.

Table 4-2. HPLC results of SSM-DPF10 samples prepared with the indicated dechlorination processing conditions.

Dechlorination	n Parameters	Dechlorination	HPLC Results	
Terminal Temperature (°C)	Profile type	and Vitrification Atmosphere	O/P	Error
400	Isothermal	Air	3.667	0.0002
400	Continuous	Air	3.667	0.0003
400	Continuous	Argon	3.620	0.0002
600	Isothermal	Air	3.658	0.001
600	Continuous	Argon	3.671	0.0005
600	Continuous	Air	3.663	0.0004

The behavior of samples during a scoping dissolution test allowed the selection of the most promising sample for additional characterization. The mass loss results are shown in Figure 4-9. SSM-DPF10-600 exhibited the most promising dissolution behavior with no measurable mass loss during the 4-day test. Two sections were selected from SSM-DPF4: one representing the

crystalline portion, and the other representing the glassy portion. The glassy portion of SSM-DPF4 performed well, while the crystalline portion dissolved rapidly. For comparison, an SSM-DP sample was also included in the scoping dissolution test; it dissolved completely before the end of the first testing period.

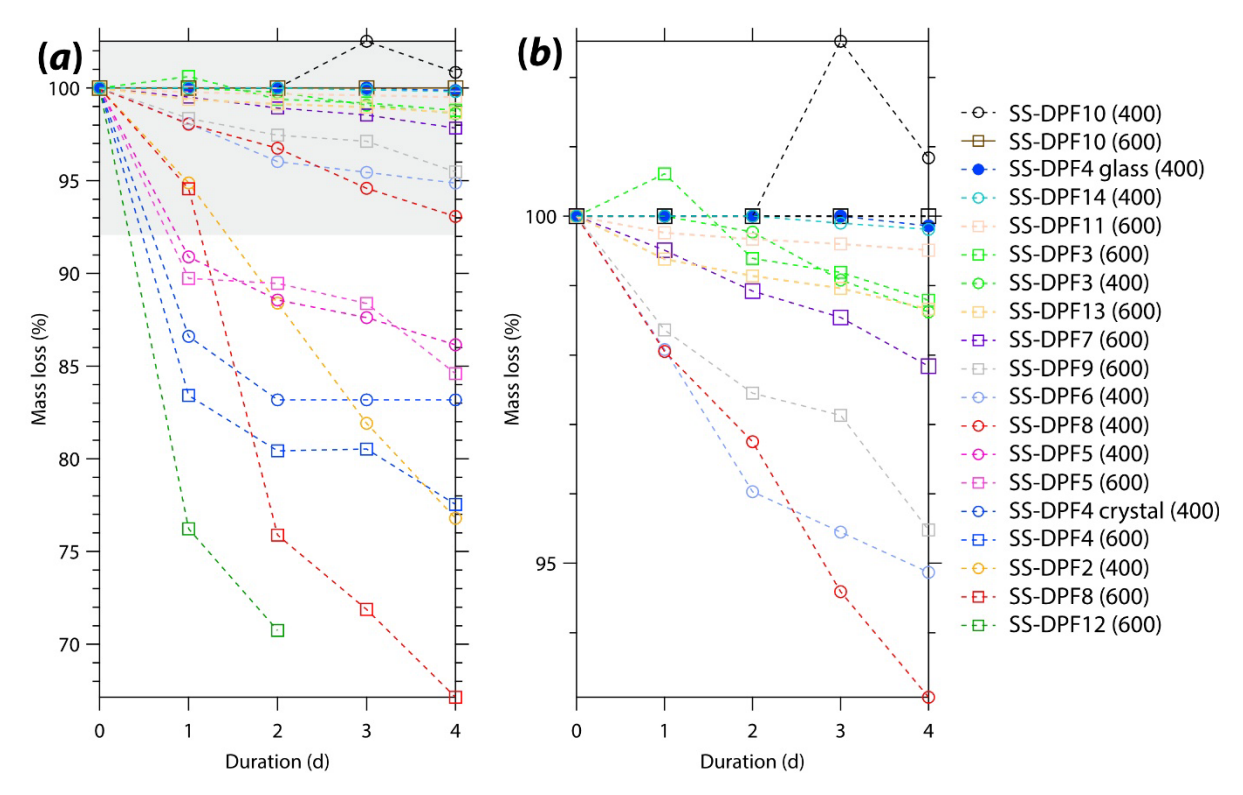


Figure 4-9. Graphs showing mass loss of SSM-DPFs in the dissolution scoping test with (a) showing all samples tested and (b) showing the magnified region of the grey area. Samples with the same composition are shown in the same color. Square markers indicate SSM-DPF-600 samples, while circular markers indicate SSM-DPF-400 samples. Two samples were tested for SSM-DPF4-400: one sample from the crystalline half, one from the glassy half, which is shown with a filled marker. SSM-DPF10-600 had no measurable mass loss during the testing period. Markers indicate measured values; dashed lines are a guide for the eye.

Dissolution tests of an SSM-DPF10-400 were conducted according to American Society for Testing and Materials International (ASTM) standard C1308. As shown in Figure 4-10, the ASTM C1308 test revealed rapid release rates for several components of SSM-DPF10. The Li, Na, and P were released at similar rates, while K was released to a slightly greater extent. The normalized loss of Si [i.e., NL(Si)] values indicate that Si released at a faster rate than other elements. NL(Fe) was an order of magnitude lower than other elements. Figure 4-11 shows the sample before and after the leach teat. The patches with an altered, light grey appearance suggest inhomogeneities in the sample that were not apparent from SEM/EDS mapping. One potential reason for this is due to Li separation and the inability for Li mapping with EDS.

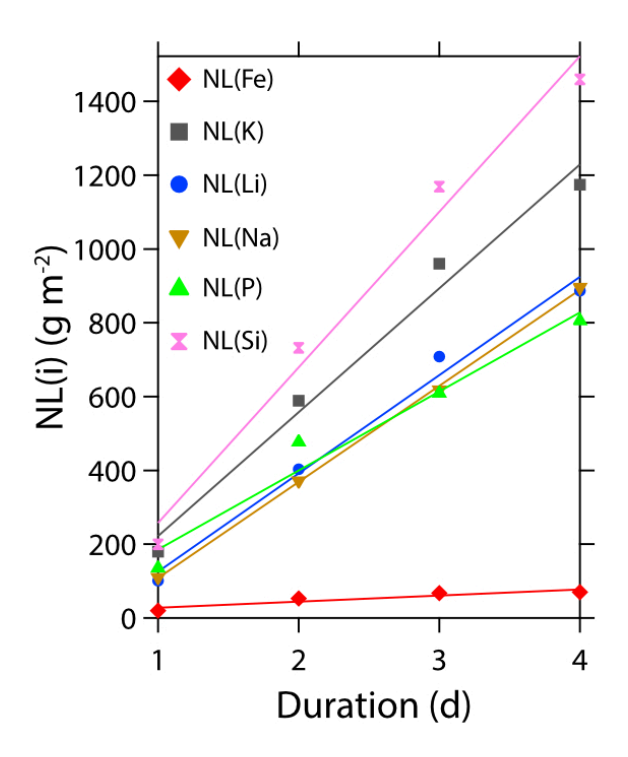


Figure 4-10. Cumulative normalized elemental mass loss values as a function of time for ASTM C1308 test with SSM-DPF10-400. The linear regression of values from each species are shown as solid lines.

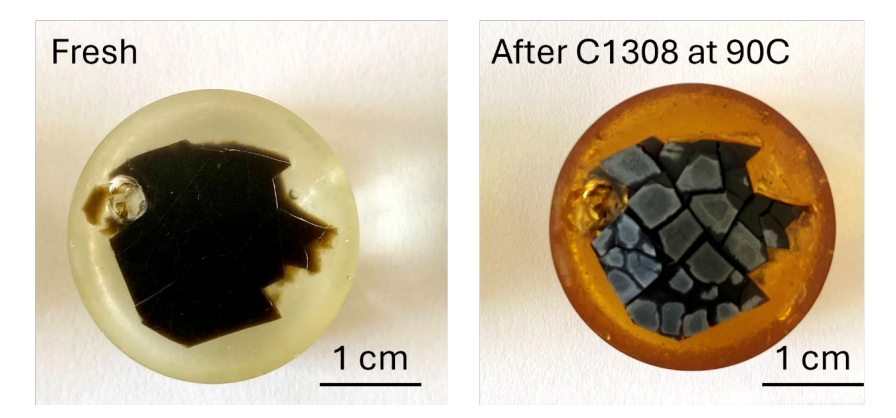


Figure 4-11. SSM-DPF10-400 before and after the ASTM C1308 leaching test. Grey spots appeared on the surface of the sample during leaching. Both samples are shown mounted in epoxy and have separate scale bars.

5.0 Summary, Conclusions, and Next Steps

Examination of H₃PO₄-based dechlorination of salt waste simulants revealed the influence of processing conditions (i.e., batch composition, atmospheric environment, temperature) on the efficacy of chlorine removal. SSM samples with a ratio of P/Cl = 1 in the starting batch were completely dechlorinated in air or argon environments by heating to 600°C. In either environment, the greatest release of Cl is concurrent with water boiling in the samples (100°C). Dechlorination occurred to a greater extent at lower temperatures in air compared to argon due to the influence of atmospheric oxygen. Above 400°C, the reaction is thermally driven, and atmosphere did not influence the extent of dechlorination achieved in the samples. Future work may investigate the potential of using isothermal holds at lower temperatures (e.g., 300°C) to achieve complete dechlorination in an air atmosphere. Complete dechlorination of the more complex ERV3 simulant was achieved in both air and argon environments with P/CI = 1.21 in the starting batch, while < 2 mass% CI remained in the P/CI = 1 samples. Monazite was detected in the samples prepared with lower P/Cl ratios, while a completely clear, amorphous sample was obtained from higher P/Cl ratios. As lanthanide phosphates (e.g., monazite and xenotime) are chemically durable phases (Chong et al. 2024), future work may investigate maximizing production of and retaining these with additional processing steps while stabilizing the alkali phosphate matrix.

Analysis of the conversion of CI from the SSM salt slurry to HCI(g) with flow rates of 2 L·min⁻¹ and heating rates of 1, 5, and 10°C·min⁻¹ suggests that while conversion of CI is greater for air at 5°C·min⁻¹. For other heating rates, the conversion of CI was greater in argon environments. Although analysis of titration data demonstrated consistently lower conversion than ICP-MS data, the relative difference between titration and ICP-MS data allowed for comparison of behavior across air and argon samples. ICP-MS and titration data differed for air samples by 40, 46, and 55 mass% for samples heated at 1, 5, and 10°C·min⁻¹, respectively. For argon samples, the variation was 32, 46, and 53 mass% for samples heated at 1, 5, and 10°C·min⁻¹, respectively. For the dechlorination module, two main parameters can be adjusted for enhanced capture, including (1) minimum carrier gas flow needed to drive the evolved species to the outlet and (2) a crucible geometry that increases exposed surface area to reduce mass-transfer limitations while keeping sufficient height to prevent overflow (e.g., due to bubbling) during gas release. The titration module can also be improved by increasing the volume of the titration cells and, if needed, using a porous sparger to enhance the gas-liquid mass transfer.

Future studies should identify operating conditions that maximize chlorine capture to close the chlorine mass balance. For the dechlorination module, two main parameters can be adjusted for enhanced capture, including (1) minimum carrier gas flow needed to drive the evolved species to the outlet and (2) a crucible geometry that increases exposed surface area to reduce mass-transfer limitations while keeping sufficient height to prevent overflow during gas release. The titration module can also be improved by increasing the volume of the titration cells and, if needed, using a porous sparger to enhance the gas-liquid mass transfer.

Silica had previously been identified as a potential material with good compatibility during ADP-based dechlorination (Riley et al. 2020). In this work, silica crucibles were observed to fracture during cooling $\approx 50\%$ of the time after dechlorination at temperatures above 400° C. Si contamination increased in the dechlorinated product at higher temperatures. Furthermore, Sirich particles were observed in iron phosphate waste forms prepared with products of dechlorination in silica crucibles. Therefore, future work will investigate the degradation of silica during H_3PO_4 -based dechlorination. Additional studies may consider other materials that had previously been studied for ADP-based dechlorination. Previous studies have identified potential

benefits of Si additions to iron phosphate glasses for salt waste immobilization (Evarts et al. 2025a; Evarts et al. 2025b), therefore Si incorporation via crucible degradation represents an interesting avenue for further investigation.

Potential containment materials (i.e., fused quartz, alumina, Monofrax K-3, SS316L, and Inconel 693) (Hsu et al. 2013; Hsu et al. 2014; Riley et al. 2020) were exposed to molten iron phosphate glass for 1 h or 4 h to analyze extents of corrosion. The type and extent of corrosion by molten iron phosphates varied depending on the chosen material. Fused guartz bars exhibited neither degradation at the melt line nor the formation of secondary phases, but iron phosphate components were detected in transverse cracks up to 200 µm deep. The surface cracks caused the bars to deteriorate during handling after the test. Alumina bars performed well, with no measurable penetration of glass components into the bar, although degradation at the melt line increased with exposure time and an iron oxide layer formed on the exposed surface. The K-3 bars showed notably higher neck corrosion for 4 h samples vs 1 h samples and significant oxide depths in the sample. Several coupons showed significant depths of penetration of the glass into the coupon interior, which is mainly attributed to the open porosity of K-3. The SS316L and Inconel 693 coupons were the worst-performing materials of those investigated here in terms of corrosion resistance. The SS316L samples had regions showing a penetration depth of glass components greater than 1 cm. Penetration into the bulk of the Inconel bars was limited to 100 µm after 1 h, but material degradation was extensive, with complete corrosion through the bulk of the Inconel sample corroded in air. SS316L bars that were exposed for 4 h were not sufficiently intact for analysis.

Dechlorinated SSM samples were vitrified with glass formers and slow cooled to determine the glass-forming region of the alkali iron phosphate compositional space and examine their properties. The glass-forming region aligns well with analogous quenched sodium iron phosphate compositions examined previously (Parsons and Rudd 2008), indicating both good thermal stability and tolerance of variation in the alkali mixture. Thermal properties (i.e., T_a , T_x , T_m) and structural properties (i.e., Fe²⁺/Fe³⁺ and O/P ratios) of the SSM-DPF10 composition showed good agreement with literature and theoretical values calculated based on the starting batches. Additionally, SSM-DPF10 samples were prepared from SSM dechlorinated with different processing conditions that were determined from studies in Section 2.0 (terminal temperature of the heating profile of 400°C or 600°C, the use of isothermal holds, heating under air or argon atmosphere) lacked significant variation in the measured O/P, indicating any of the selected processing conditions used for dechlorination are acceptable to achieve a consistent O/P in the final waste form. Additional work may examine other thermal and structural properties along with greater variation in the dechlorination processing parameters, including the use of a more complex salt simulant such ERV3, as to determine the nature and extent of their impact on the final waste form. Chemical durability tests on the SSM-DPF10 composition selected for this work showed rapid releases of all components. Therefore, future studies may expand on the compositions selected for investigation of the influence of dechlorination processing parameters.

6.0 References

Barnes, D, N Rood, C Andersen, and MF Simpson. 2025. "Gas–solid synthesis of UCl₃ using ammonium chloride and uranium hydride." *Journal of Radioanalytical and Nuclear Chemistry* **334**(5):3729–40.

Beland, J. 2025. "Processing Parameters and Kinetics of Phosphate-Based Dechlorination for Electrorefiner Salt Waste." University of Nevada Reno, ProQuest One Academic: Master's Thesis.

Brow, RK, CW Kim, and ST Reis. 2020. "Iron polyphosphate glasses for waste immobilization." *International Journal of Applied Glass Science* **11**(1):4–14.

Chong, S and BJ Riley. 2024. "Compositional effects on the chemical durabilities of aluminophosphate glasses: A review." *Journal of Non-Crystalline Solids: X* **21**:100205.

Chong, S, BJ Riley, X Lu, J Du, T Mahadevan, and V Hegde. 2024. "Synthesis and properties of anhydrous rare-earth phosphates, monazite and xenotime: a review." *RSC Advances* **14**(27):18978–9000.

Day, D, Z Wu, C Ray, and P Hrma. 1998. "Chemically Durable Iron Phosphate Glass Waste forms." *Journal of Non-Crystalline Solids* **241**(1):1–12.

Dong, Y, K Xu, Z Jia, C Niu, and D Xu. 2022. "Dechlorination and vitrification of electrochemical processing salt waste." *Journal of Nuclear Materials* **567**:153833.

Evarts, JS, BJ Riley, CE Lonergan, MS Harris, J Bai, E Bohannan, I Ajoku, S Chong, and JS McCloy. 2025a. "Synergy in Materials: Leveraging Phosphosilicate Waste Forms for Electrochemical Salt Waste." *ACS Sustainable Resource Management* **2**(3):514–23.

Evarts, JS, HS Werth, BJ Riley, K Carlson, and M Simpson. 2025b. "Phosphate-Based Approaches for Dechlorination and Treatment of Salt Waste from Electrochemical Processing of Used Nuclear Fuel: A Perspective on Recent Work." *ACS Omega* (doi: 10.1021/acsomega.5c08801).

Fang, X, CS Ray, and DE Day. 2003. "Glass transition and fragility of iron phosphate glasses.: II. Effect of mixed-alkali." *Journal of Non-Crystalline Solids* **319**(3):314–21.

Hsu, J-H, JW Newkirk, C-W Kim, RK Brow, ME Schlesinger, CS Ray, and DE Day. 2014. "The performance of Inconel 693 electrodes for processing an iron phosphate glass melt containing 26wt.% of a simulated low activity waste." *Journal of Nuclear Materials* **444**(1):323–30.

Hsu, J-H, JW Newkirk, C-W Kim, CS Ray, RK Brow, ME Schlesinger, and DE Day. 2013. "Corrosion of Inconel 690 and Inconel 693 in an iron phosphate glass melt." *Corrosion Science* **75**:148–57.

Marcial, J, S Chong, BJ Riley, RK Brow, JD Vienna, CW Kim, and M Tang. 2024. *Bonding Environments and Radiation Stabilities of Phosphate Glasses*. PNNL-35754, Pacific Northwest National Laboratory, Richland, WA.

References 52

Murray, P, H Werth, S Sullivan, BJ Riley, M Simpson, C Lonergan, and K Carlson. 2024. "Phosphate-based dechlorination of electrorefiner salt waste using a phosphoric acid precursor." *ACS Omega* **9**(17):19395–400.

Parsons, AJ and CD Rudd. 2008. "Glass forming region and physical properties in the system P₂O₅-Na₂O–Fe₂O₃." *Journal of Non-Crystalline Solids* **354**(40):4661–67.

Riley, BJ and S Chong. 2022. "Dehalogenation reactions between halide salts and phosphate compounds." *Frontiers in Chemistry* **10**:976781.

Riley, BJ, S Chong, and CE Lonergan. 2021a. "Dechlorination Apparatus for Treating Chloride Salt Wastes: System Evaluation and Scale-Up." *ACS Omega* **6**(47):32239–52.

Riley, BJ, S Chong, and ET Nienhuis. 2023. *Canister Centerline Cooling Experiments for DPF5-336 Reference Material Made with ERV3b Salt Simulant*. PNNL-33802, Pacific Northwest National Laboratory, Richland, WA.

Riley, BJ, JA Peterson, JD Vienna, WL Ebert, and SM Frank. 2020. "Dehalogenation of electrochemical processing salt simulants with ammonium phosphates and immobilization of salt cations in an iron phosphate glass waste form." *Journal of Nuclear Materials* **529**:151949.

Riley, BJ, JD Vienna, and WL Ebert. 2021b. *Road Map for Developing Iron Phosphate Waste Forms for Salt Wastes*. PNNL-30998, ANL/CFCT-20/44, Pacific Northwest National Laboratory, Richland, WA.

Rood, N, C Andersen, K Carlson, and MF Simpson. 2024. "Chlorination of Li₂O and uranium metal in molten LiCl–KCl using NH₄Cl." *Journal of Radioanalytical and Nuclear Chemistry* **333**(8):4353–66.

Shelby, JE. 1975. "Thermal expansion of mixed-alkali germanate glasses." *Journal of Applied Physics* **46**(1):193–96.

Tarani, E and K Chrissafis. 2024. "Isoconversional methods: A powerful tool for kinetic analysis and the identification of experimental data quality." *Thermochimica Acta* **733**:179690.

Vyazovkin, S and CA Wight. 1999. "Model-free and model-fitting approaches to kinetic analysis of isothermal and nonisothermal data." *Thermochimica Acta* **340-341**:53–68.

Werth, H, J Beland, P Murray, D Liang, L Sharpless, J Evarts, C Lonergan, BJ Riley, M Simpson, and K Carlson. 2025. "Evaluation of Processing Conditions for the Reduction of Electrochemical Salt Waste Using Phosphate-Based Dechlorination." *ACS ES&T Engineering* **5**(10):2667–79.

References 53

Appendix A – Additional Characterization Data

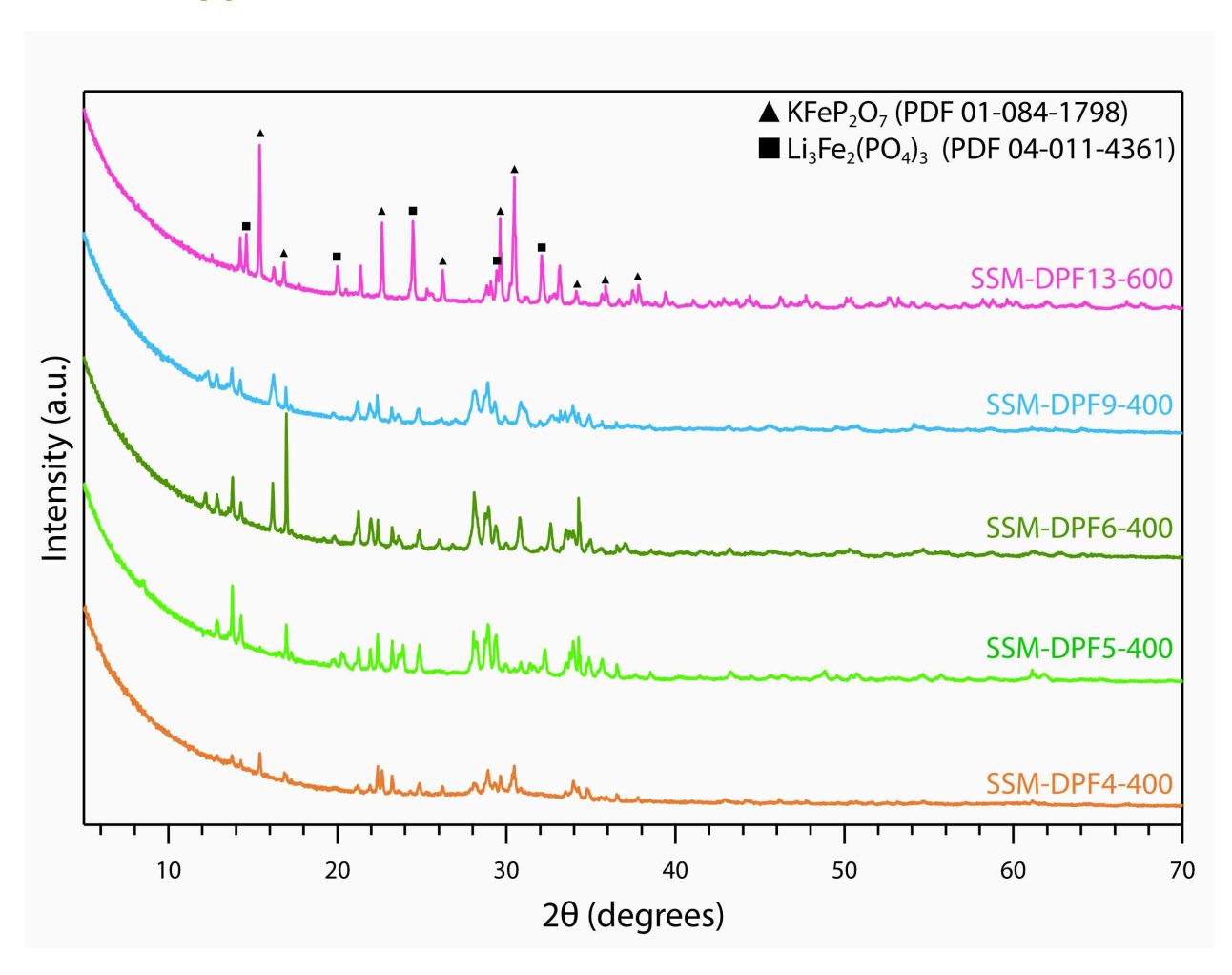


Figure A-1. Waterfall plot of XRD scans of SSM-DPFs shows crystallized samples as labelled. Bruker AXS DIFFRAC^{plus} EVA was used to identify the crystalline phases present in the samples. Markers show peak assignments.

Appendix A A.1

Pacific Northwest National Laboratory

902 Battelle Boulevard P.O. Box 999 Richland, WA 99354

1-888-375-PNNL (7665)

www.pnnl.gov